A POTENTIAL METHOD FOR PRECISION POSITION SELF-SENSING IN VOICE-COIL ACTUATORS

A Thesis

by

ROBERT SAMUEL LIPHAM

Submitted to the Office of Graduate and Professional Studies of
Texas A&M University
in partial fulfillment of the requirements for the degree of

MASTER OF SCIENCE IN MECHANICAL ENGINEERING

Chair of Committee,	Won-jong Kim
Committee Members,	Alan Palazzolo
	Hamid Toliyat
Head of Department,	Andreas A. Polycarpou

December 2020

Major Subject: Mechanical Engineering

ABSTRACT

An approach for self-sensing is proposed for voice-coil actuators that have an invertible, position-dependent inductance. Actuators with these properties are denoted as position-invertible, variable-inductance (PIVI) actuators. The self-sensing methodology is based on tracking the inductance of a PIVI actuator from the oscillation frequency of a modified Pierce oscillator. By extension, the oscillation frequency provides a measurement of the actuator position without an external position sensor.

An electrical model for PIVI voice-coil actuators is first derived to aid in analysis. Oscillator theory is then introduced and applied to the analysis of a typical Pierce oscillator. The modified Pierce oscillator is then introduced and analyzed under the assumption of low-frequency actuator motion and driving current relative to the oscillation frequency. The effects of parasitic capacitance from the actuator current source are then discussed along with a mitigation method. A test circuit, including the modified Pierce oscillator and a transconductance amplifier, is then presented. Due to time constraints, the modified Pierce oscillator was constructed with a variable inductor rather than an actual PIVI actuator. This was considered acceptable since the variable inductor mimics a PIVI actuator operating under the low-frequency assumption. Modifications to the transconductance amplifier were presented that allowed parasitic impedance to be increased by a minimum factor of three.

The modified Pierce oscillator circuit was tested under conditions that simulated a powered PIVI actuator. Results showed the oscillation frequency was an invertible function of the core-insertion distance of the variable inductor. It was also observed that the oscillation frequency varied less

than 3% in the presence of various disturbance currents through the variable inductor. The tested conditions simulated a powered PIVI actuator, so it was considered likely that these two behaviors would also be observed if the modified Pierce oscillator was used with an actual PIVI actuator. While these results are not definitive, they suggest that the modified Pierce oscillator could be used as a self-sensing methodology for PIVI type voice-coil actuators. However, more work will be needed to verify this behavior with an actual PIVI type voice-coil actuator.

DEDICATION

In memory of my grandfather who was a strong believer in higher education and lifelong learning.

ACKNOWLEDGMENTS

I would like to thank my advisor, Dr. Won-jong Kim, for his consistent mentorship and support throughout my research. I would also like to thank Dr. Alan Palazzolo and Dr. Hamid Toliyat for serving on my committee. Finally, I would like to thank my friends and family for their support.

CONTRIBUTORS AND FUNDING SOURCES

Contributors

This work was supervised by a thesis committee consisting of Professor Won-jong Kim and Professor Alan Palazzolo of the Department of Mechanical Engineering and Professor Hamid Toliyat of the Department of Electrical and Computer Engineering.

The use of a push-pull transconductance amplifier came from the suggestion of Erwin Thomas. All other work conducted for the thesis was completed by the student, under the supervision of Professor Won-jong Kim of the Department of Mechanical Engineering.

Funding Sources

Research was performed with the use of Dr. Won-jong Kim's research laboratory and instrumentation. The project was self-funded by the student with the support of a Graduate Assistant Teaching position unrelated to the project.

TABLE OF CONTENTS

Page

ABSTRACT ii

DEDICATION iv

ACKNOWLEDGMENTS v

CONTRIBUTORS AND FUNDING SOURCES vi

TABLE OF CONTENTS vii

LIST OF FIGURES ix

LIST OF TABLES xi

1. INTRODUCTION 1

1.1 Overview 1

1.2 Literature Review 2

1.3 Contributions of this Thesis 3

2. ELECTRICAL MODEL FOR PIVI VOICE-COIL ACTUATORS..... 5

2.1 Section Overview 5

2.2 Planar E-Core Actuator 5

3. ANALYSIS OF A MODIFIED PIERCE OSCILLATOR FOR SELF-SENSING 14

3.1 Section Overview 14

3.2 Oscillator Fundamentals 14

3.3 Analysis of a Typical Pierce Oscillator 16

3.4 Modified Pierce Oscillator 25

3.5 Parasitic Capacitance 34

4. EXPERIMENTAL VALIDATION OF THE MODIFIED PIERCE OSCILLATOR 41

Page

4.1 Section Overview 41

4.2 Experimental Apparatus 41

4.3 Experimental Procedure 59

4.4 Results 62

4.5 Practical Limitations 65

5. SUMMARY AND CONCLUSIONS 68

5.1 Summary 68

5.2 Conclusions 68

6. FUTURE WORK 70

REFERENCES 71

APPENDIX A: EXPERIMENTAL MEASUREMENT OF INDUCTANCE 72

APPENDIX B: THEORETICAL IMPEDANCE PLOT GENERATION..... 79

APPENDIX C: MATLAB DATA REDUCTION SCRIPT..... 80

LIST OF FIGURES

FIGURE		Page
2.1	Diagram of a planar E-core actuator	5
2.2	Depiction of the Ampere loop through the core	9
3.1	A generic oscillator feedback loop	15
3.2	Circuit diagram of a typical Pierce oscillator	17
3.3	Depiction of a typical Pierce oscillator circuit using a voltage-controlled voltage source model for the op amp	17
3.4	Rearranged circuit from Figure 3.3	18
3.5	Feedback gain elements from Figure 3.4	19
3.6	Circuit diagram of a modified Pierce oscillator	26
3.7	Depiction of the actuator and oscillator frequency-bands	27
3.8	Simplified circuit model of the modified Pierce oscillator	28
3.9	Updated circuit model of the modified Pierce oscillator	29
3.10	Circuit diagram of the modified Pierce oscillator with parasitic capacitance from the current source	35
3.11	Circuit diagram of the modified Pierce oscillator with a compensated current source	36
3.12	Isolated components of the compensated current source	37
3.13	Comparison of the normalized magnitude of impedance of the compensated current source and the parasitic capacitance alone	39
4.1	Diagram of the test circuit	42
4.2	Implementation of the test circuit in Figure 4.1	43
4.3	Power supply arrangement	44
4.4	Detailed view of the modified Pierce oscillator portion of Figure 4.1	45

FIGURE Page

4.5 Implementation of the modified Pierce oscillator 46

4.6 Image of the variable inductor 47

4.7 Depiction of the core-insertion-distance measurement methodology 48

4.8 Plot of inductance vs. core-insertion distance for the variable inductor 49

4.9 Predicted fundamental oscillation frequency of the modified Pierce oscillator as a function of core-insertion distance 51

4.10 Detailed view of the transconductance amplifier portion of Figure 4.1 52

4.11 Implementation of the transconductance amplifier 53

4.12 Depiction of a conventional transconductance amplifier with parasitic capacitance 54

4.13 Parallel circuit elements from Figure 4.12 55

4.14 Comparison of the magnitude of theoretical impedance of the parasitic capacitance, compensated path, and variable inductor 57

4.15 Comparison of design gain with measured transconductance amplifier gain .. 58

4.16 View of full test setup 60

4.17 Comparison of oscillation frequency as a function of core-insertion distance from all four excitation tests 63

4.18 Comparison of the percentage error of the DC, sine-wave, and square-wave excitation tests from the quiescent-output test 64

4.19 Comparison of oscillation frequency as a function of core-insertion distance from the free-oscillation test, quiescent-output test, and predicted fundamental oscillation frequency 65

4.20 Comparison of the percentage error of the quiescent-output test and free-oscillation test from the predicted fundamental oscillation frequency 66

A.1 Circuit diagram of the low-pass filter used to determine inductance 72

A.2 Comparison of regression equation with test data from Table A.1 78

LIST OF TABLES

TABLE		Page
4.1	Summary of oscillator component values	50
4.2	Summary of theoretical impedances at the oscillator frequency-band boundaries	58
A.1	Summary of experimental inductance data	77

1. INTRODUCTION

1.1 Overview

In many applications, voice-coil actuators offer a simple and compact solution for linear motion. The footprint of voice-coil actuators often includes a separate position sensor for feedback control. The elimination of this position sensor, with the application of a self-sensing methodology, can help to produce an actuator with a smaller footprint and greater mechanical reliability. A particular subset of voice-coil actuators is of interest for self-sensing applications. This subset is defined by two primary requirements. First, the inductance of the actuator must vary with position over a useful range of the actuator's motion. Second, the functional relationship between inductance and position must be strictly monotonic over this range of motion. The result of these two requirements is that the position of a voice-coil actuator in this subset can be uniquely determined from its inductance. For both simplicity and consistency, voice-coil actuators within this subset are referred to as position-invertible, variable-inductance (PIVI) actuators.

The self-sensing methodology being presented is based on the behavior of a Pierce oscillator with a source of variable-inductance. As is discussed in more detail in Section 3, this class of oscillators has a useful property in that the fundamental oscillation frequency can be controlled by a single inductor. If the structure of the Pierce oscillator is slightly modified and the inductor is replaced with a PIVI type actuator, the fundamental frequency of oscillation will theoretically be dependent on the position of the actuator.

1.2 Literature Review

Many of the current self-sensing methodologies employed with voice-coil or solenoid actuators are based on measuring the inductance of the actuator since it is, typically, dependent on the position of the actuator. There are innumerable ways of measuring the inductance of the actuator during operation, but a couple are reviewed here. Rahman *et al.* [1] discussed a method by which the inductance of a solenoid actuator was estimated from the current rise due to an applied pulse-width-modulation (PWM) voltage. This estimated inductance was then compared to a lookup table of the solenoid inductance as a function of current and position. As long as the current through the actuator was known, the position of the actuator could be estimated every PWM cycle.

Wu and Chen [2] presented a solenoid valve actuator which was modified by the addition of an external capacitor. An excitation signal, near the expected natural frequency of the LC circuit, was injected during operation. Assuming the external capacitance remained constant, the inductance was estimated by measuring the phase angle of the capacitor voltage compared to the input voltage. This estimated inductance was then compared to a position-calibration table for the actuator. Measurement during powered operation was achieved by using two of these solenoids and delegating position estimation to the unpowered solenoid.

Moore and Moheimani [3] described a very similar methodology to the one presented in this thesis, but applied to a micro-electro-mechanical systems (MEMS) comb actuator. The comb actuator was placed within the resonant circuit of a Pierce oscillator. Because the capacitance of the comb actuator is position-dependent, the fundamental oscillation frequency of the Pierce oscillator was dependent on position. Therefore, the position of the actuator could be estimated from the

fundamental oscillation frequency. This methodology is not entirely comparable with the methodology presented in this thesis since their actuator is capacitive and operates on an entirely different scale. This allows the oscillator to work in the MHz frequency range, and also allows the use of a voltage source to power the actuator. However, the range of motion and force output are necessarily limited by the size of the actuator. By comparison, the modified Pierce oscillator presented in this thesis is applied to inductive, voice-coil actuators that operate on a much larger scale. While both the force output and range of motion are larger in these types of actuators, the modified Pierce oscillator can only operate in the kHz frequency range due to core losses. A current source, in the form of a transconductance amplifier with modifications for parasitic capacitance mitigation, is also required to ensure the oscillator is not affected by the impedance of the actuator power source.

1.3 Contributions of this Thesis

The primary contribution of this thesis is the development of a potential methodology for precision position self-sensing in voice-coil actuators. Self-sensing is achieved by placing a voice-coil actuator within the resonant feedback path of a modified Pierce oscillator. The inductance of the actuator is directly related to the position of the actuator and controls the oscillation frequency of the modified Pierce oscillator. Therefore, the oscillation frequency can be used to determine the actuator position.

A secondary contribution of this thesis is the development of a parasitic capacitance compensation methodology for the transconductance amplifier used in this research. Passive compensation components are placed between the isolated ground connections of the push-pull stages and allow the output impedance of the amplifier to be increased in certain frequency-bands. This

methodology can be adapted for use in typical transconductance amplifiers by placing the compensation components in series with the output.

2. ELECTRICAL MODEL FOR PIVI VOICE-COIL ACTUATORS

2.1 Section Overview

Since the position of PIVI actuators can theoretically be determined from the inductance, it is possible to develop a self-sensing methodology based on measuring the inductance during operation. However, before a methodology can be considered, a representative electrical model is needed for PIVI actuators. To this end, an example actuator is analyzed. The resulting electrical model is then generalized for PIVI actuators.

2.2 Planar E-Core Actuator

A planar E-core voice-coil actuator, shown in Figure 2.1, is analyzed to find a representative electrical model for PIVI actuators. Note that the actuator has depth d into the page.

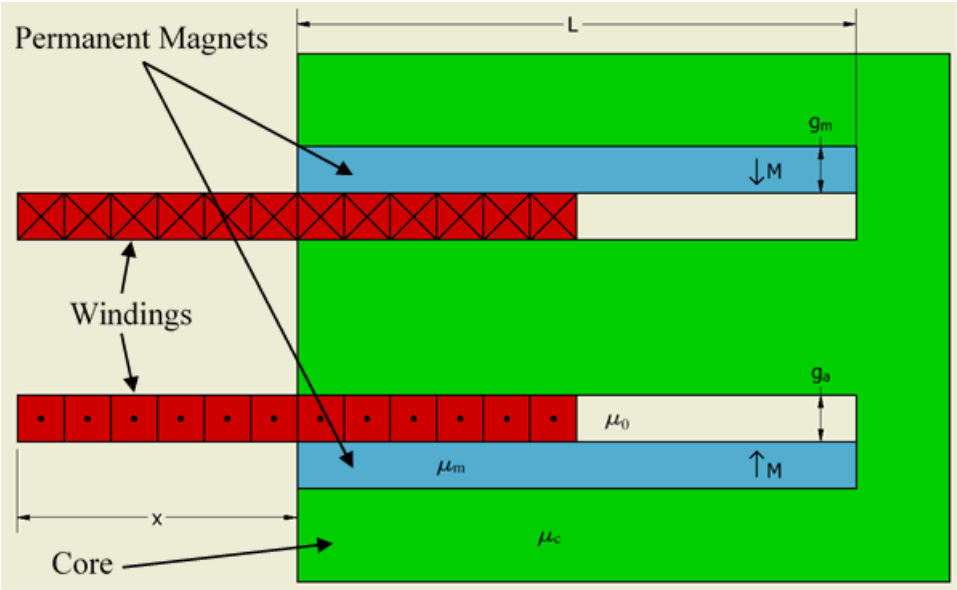

Figure 2.1: Diagram of a planar E-core actuator.

The core, shown in green, has permeability μ_c. The core has a gap on both sides of the center with length L and thickness $g_m + g_a$. The windings, shown in red, have N_T evenly distributed turns that fit within the gap. Note that both the gap and windings have the same length L. An excitation current I flows through the windings. The windings can only move relative to the core along the horizontal axis of the diagram. This relative displacement is referred to as the actuator position and is denoted by x. The permanent magnets, shown in blue, have a magnetization intensity of M and permeability μ_m. The space surrounding the actuator is assumed to have the permeability of free space μ_0.

2.2.1 Magnetoquasistatic Approximations

Several assumptions are made in the analysis of this actuator. Primary among these are the magnetoquasistatic (MQS) approximations [4]. First, it is assumed that the electric fields in the actuator are negligible, and that the magnetic fields in the actuator are significant. For this actuator, there are no significant sources of charge or electric field, and the magnetic fields produced by the permanent magnets and windings are significant. Therefore, the electric fields are ignored, and only the magnetic fields are modeled in the analysis.

Second, it is assumed that the product of the operating frequency and characteristic length of the actuator is much smaller than the speed of light [4]

$$\omega L_c \ll c \tag{2.1}$$

where ω is the operating frequency of the actuator in rad/s, L_c is the characteristic length of the actuator in meters, and c is the speed of light in m/s. If the condition of (2.1) is met, then propagation effects can be ignored. For this actuator, if a maximum operating frequency of 100

kHz (628×10^3 rad/s) and maximum characteristic length of 10 cm are assumed, then the resulting product is 62.8×10^3 m/s. This is much less than the speed of light, so the quasistatic approximation is valid.

The MQS approximations result in the quasistatic form of Maxwell's equations for magnetic fields with an added continuity constraint [4]

$$\oint_C \boldsymbol{H} \cdot d\boldsymbol{l} = \int_S \boldsymbol{J} \cdot d\boldsymbol{a} = I_{net} \tag{2.2}$$

$$\oint_S \boldsymbol{B} \cdot d\boldsymbol{a} = 0 \tag{2.3}$$

$$\oint_S \boldsymbol{J} \cdot d\boldsymbol{a} = 0 \tag{2.4}$$

where (2.2) is the static form of Ampere's law, and (2.3) is Gauss's law for magnetic fields. Equation (2.4) requires zero current flux through the surface of a closed volume. This eliminates the possibility of charge collection within the system and therefore violation of the MQS approximations. The flux density in (2.3) is defined by (2.5)

$$\boldsymbol{B} = \mu_{mat}(\boldsymbol{H} + \boldsymbol{M}) \tag{2.5}$$

where μ_{mat} is the magnetic permeability of the material, $\boldsymbol{H}$ is the magnetic field intensity, and $\boldsymbol{M}$ is the magnetization of the material.

2.2.2 Additional Assumptions

In addition to the MQS approximations, several other simplifying assumptions are made in this analysis. The first major assumption is that the core material has an infinite magnetic permeability

compared to vacuum. For materials like ferrite and silicon steel, the relative permeability can be as much as 5,000, so this assumption is not entirely unrealistic. If the material is magnetically soft, as is typically the case with highly permeable materials, the magnetization of the material can be assumed to be negligible. This results in (2.5) simplifying to

$$\boldsymbol{B} = \mu_{mat}\boldsymbol{H}. \tag{2.6}$$

In the limit of infinite permeability, (2.6) requires that the magnetic field intensity go to zero in order for the flux density to be finite. Therefore, because the permeability of the core is assumed to be effectively infinite, the magnetic field intensity inside the core is assumed to be zero.

This infinite permeability leads to several underlying assumptions that must be addressed. Primary among these is that the core does not saturate. If core saturation does occur, then the permeability can decrease significantly, and the resulting field intensity inside the core can be non-negligible. In addition to this, the behavior of the core is assumed to be both frequency-invariant and lossless. If either of these conditions are violated, it would mean a non-negligible field intensity exists within the core.

The second major assumption is that the depth d and distance L are much larger than the gap formed by g_a and g_m. If this is the case, the magnetic fields within the gap will be much stronger than the fringing fields at the edges of the core. Therefore, it is assumed that the magnetic fields are concentrated within the gap, and that the fringing fields are negligible.

The last major assumption is that the actuator position, x, is always much smaller than L. The result of this assumption is that the majority of the windings are always concentrated within the

gap. Consequently, these windings will be the most significant contributor to the magnetic field within the gap and, by extension, both the inductance and force output of the actuator. In contrast, the windings outside of the gap will not contribute as significantly to the actuator's characteristic since the magnetic fields produced by these windings are not as concentrated. Additionally, modeling the magnetic field outside of the core gap is not a trivial process due to the lack of a well-defined flux path. Therefore, so long as $x \ll L$, the modelling is simplified by assuming that the windings outside of the core gap have a negligible effect on the characteristics of the actuator.

2.2.3 Magnetic Analysis

An Ampere loop is defined through the actuator core, permanent magnet, and air gap as shown in Figure 2.2. The left vertical leg of the Ampere loop exists at a horizontal distance x' from the left end of the core. The remaining legs of the loop reside along the center of the core.

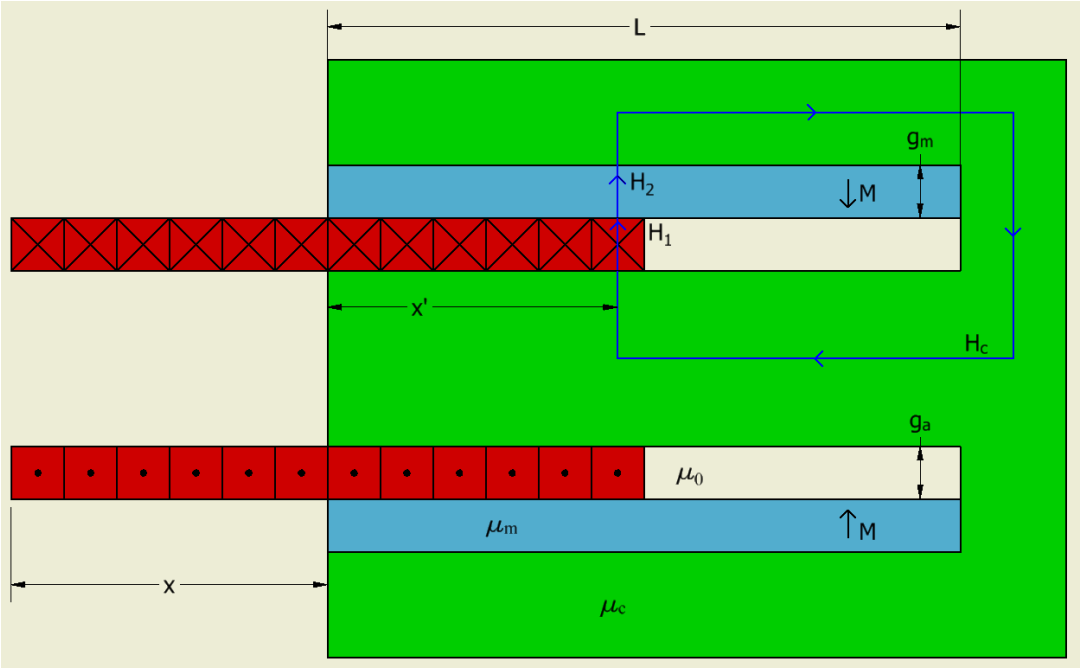

Figure 2.2: Depiction of the Ampere loop through the core.

Three magnetic field intensities are defined around the loop. H_1 is the field intensity inside the air gap, H_2 is the field intensity inside the permanent magnet, and H_c is the field intensity inside the core. H_1 and H_2 are assumed to be constant over their respective vertical distances, and H_c is assumed to be constant over a mean core length L_{mc}. Applying the static form of Ampere's law in (2.2) results in (2.7).

$$\oint_C \boldsymbol{H} \cdot d\boldsymbol{l} = H_1(x,x')g_a + H_2(x,x')g_m + H_c L_{mc} = I_{net} \tag{2.7}$$

The field inside the core is assumed to be zero from the infinite permeability assumption, so (2.7) simplifies to (2.8).

$$H_1(x,x')g_a + H_2(x,x')g_m = I_{net} \tag{2.8}$$

In order to define I_{net}, the number of windings enclosed by the loop must be known as a function of x and x'. This winding function is defined in (2.9).

$$N(x,x') = \begin{cases} \frac{N_T}{L}\left((L-x)-x'\right); & 0 \le x' \le (L-x) \\ 0; & (L-x) < x' \le L \end{cases} \tag{2.9}$$

where N_T is the total number of tuns in the solenoid. Note that the winding function ignores the windings outside of the core gap due to the implications of the assumption that $x \ll L$: It is assumed that the windings outside of the core gap have a negligible effect on the behavior of the actuator. I_{net} is now redefined in (2.8) as

$$H_1(x,x')g_a + H_2(x,x')g_m = N(x,x')I. \tag{2.10}$$

Gauss's law is now applied to the volume enclosed by the air gap.

$$\oint_S \boldsymbol{B} \cdot d\boldsymbol{a} = -\mu_0 d\int_0^L H_1(x,x')dx' + \mu_m d\int_0^L (H_2(x,x') - M)dx' = 0 \tag{2.11}$$

Simplifying (2.11) results in (2.12).

$$\frac{\mu_0}{\mu_m}\int_0^L H_1(x,x')dx' = \int_0^L (H_2(x,x') - M)dx'. \tag{2.12}$$

The integrands cancel on both sides of (2.12). Solving for $H_2(x,x')$ results in

$$H_2(x,x') = \frac{\mu_0}{\mu_m}H_1(x,x') + M. \tag{2.13}$$

Substituting (2.13) into (2.10) and solving for $H_1(x,x')$ yields

$$H_1(x,x') = \frac{N(x,x')I - g_m M}{g_a + \frac{\mu_0}{\mu_m}g_m}. \tag{2.14}$$

The flux linkage is defined as

$$\lambda(x,I) = \int_S N\boldsymbol{B}\cdot d\boldsymbol{a} = \mu_0 d\int_0^L N(x,x')H_1(x,x')dx'. \tag{2.15}$$

Substituting (2.14) into (2.15) yields (2.16).

$$\lambda(x,I) = \frac{\mu_0 d}{g_a + \frac{\mu_0}{\mu_m}g_m}\left(I\int_0^L N^2(x,x')dx' - g_m M\int_0^L N(x,x')dx'\right) \tag{2.16}$$

Substituting (2.9) into (2.16) results in (2.17).

$$\begin{aligned}\lambda(x,I) = \frac{d}{\frac{g_a}{\mu_0} + \frac{g_m}{\mu_m}}\Bigg(&\frac{N_T^2 I}{L^2}\left(\int_0^{L-x}\left((L-x)-x'\right)^2 dx' + \int_{L-x}^{L} 0\cdot dx'\right)\\ &-\frac{g_m M N_T}{L}\left(\int_0^{L-x}\left((L-x)-x'\right)dx' + \int_{L-x}^{L} 0\cdot dx'\right)\Bigg)\end{aligned} \tag{2.17}$$

Integrating (2.17) yields (2.18).

$$\lambda(x,I)=\frac{N_T d}{L\left(\frac{g_a}{\mu_0}+\frac{g_m}{\mu_m}\right)}\left(\frac{N_T I}{L}\left((L-x)^2x'-(L-x)x'^2+\frac{1}{3}x'^3\right)\right.$$
$$\left.-g_m M\left((L-x)x'-\frac{1}{2}x'^2\right)\right)\Big|_0^{L-x} \tag{2.18}$$

Simplifying (2.18) results in the final equation for the flux linkage

$$\lambda(x,I)=\frac{N_T d}{L\left(\frac{g_a}{\mu_0}+\frac{g_m}{\mu_m}\right)}\left(\frac{N_T}{3L}(L-x)^3 I-\frac{g_m M}{2}(L-x)^2\right). \tag{2.19}$$

The terminal voltage is now found by taking the derivative of the flux linkage with respect to time.

$$V=\frac{d\lambda(x,I)}{dt}=\frac{N_T d}{L\left(\frac{g_a}{\mu_0}+\frac{g_m}{\mu_m}\right)}\left(\frac{N_T}{3L}\left(3(L-x)^2 I(-\dot{x})+(L-x)^3\dot{I}\right)\right.$$
$$\left.-\frac{g_m M}{2}\left(2(L-x)(-\dot{x})\right)\right) \tag{2.20}$$

Collecting the like terms of (2.20) results in

$$V=\frac{N_T d}{L\left(\frac{g_a}{\mu_0}+\frac{g_m}{\mu_m}\right)}\left(\frac{N_T}{3L}(L-x)^3\dot{I}+\left(g_m M(L-x)-\frac{N_T}{L}(L-x)^2 I\right)\dot{x}\right). \tag{2.21}$$

Two new terms are now defined from (2.21)

$$L_a(x)\triangleq\frac{N_T^2 d(L-x)^3}{3L^2\left(\frac{g_a}{\mu_0}+\frac{g_m}{\mu_m}\right)} \tag{2.22}$$

$$K_e(x,I)\triangleq\frac{N_T d(L-x)}{L\left(\frac{g_a}{\mu_0}+\frac{g_m}{\mu_m}\right)}\left(g_m M-\frac{N_T}{L}(L-x)I\right) \tag{2.23}$$

where (2.22) defines the inductance of the actuator, and (2.23) defines the back emf of the actuator.

It is clear from (2.22) that the E-core actuator has a position-dependent inductance that is strictly monotonic over the range of actuator motion. Therefore, the E-core actuator meets the PIVI actuator requirements. If the winding resistance is included, then the full electrical model of this actuator can be written as

$$V\left(x, \dot{x}, I, \dot{I}\right) = RI + L_a(x)\dot{I} + K_e(x, I)\dot{x}. \tag{2.24}$$

While (2.22) and (2.23) are specific to the E-core design, (2.24) can be more generally applied to PIVI actuators. That is to say, the terminal voltage of a PIVI actuator can typically be modelled by the series combination of a winding resistance, position-varying inductance, and back emf voltage source.

2.2.4 Challenges for Self-Sensing

Equation (2.24) clearly shows that the terminal voltage of PIVI actuators is not purely described by a variable-inductance. Indeed, both the series winding resistance and back emf affect the terminal voltage. While the effect of the series winding resistance can typically be accounted for or neglected, the back emf can dominate the terminal voltage if the motion of the actuator is fast enough. A further complication arises when the power source for the actuator is considered. Both the impedance and signal output of the power source can affect the ability to measure the inductance. Therefore, a potential self-sensing method needs to measure the inductance while rejecting the effects of both the back emf and the power source used to drive the actuator. The following section discusses the theoretical background for a modified Pierce oscillator that meets these requirements under certain constraints.

3. ANALYSIS OF A MODIFIED PIERCE OSCILLATOR FOR SELF-SENSING

3.1 Section Overview

As was discussed in the previous section, the strictly monotonic inductance of PIVI actuators makes it theoretically possible to uniquely determine an actuator's position by measuring its inductance. In this section, a modified Pierce oscillator is discussed that can be used for self-sensing with PIVI actuators. The modifications in this circuit allow the effects of the back emf and a power source to be ignored under certain operating constraints. The result is an oscillator with a fundamental frequency that depends on the inductance of a PIVI actuator.

Before the modified Pierce oscillator is considered, an overview of oscillator fundamentals is presented to aid in the analysis. These fundamentals then are applied to the analysis of a typical Pierce oscillator to show the benefits of this topology. The modified Pierce oscillator is then discussed and analyzed to show how it can be used for self-sensing. The effect and mitigation of parasitic capacitance in the modified Pierce oscillator is then discussed.

3.2 Oscillator Fundamentals

A generic oscillator feedback loop is shown in Figure 3.1 [5]. $A(j\omega)$ is the amplifier voltage gain, and $B(j\omega)$ is the feedback gain that describes the transfer function of the feedback network. The closed-loop transfer function for this positive feedback loop is defined by (3.1).

$$\frac{V_o}{V_i} = \frac{A(j\omega)}{1 - A(j\omega)B(j\omega)} \tag{3.1}$$

Where the term $A(j\omega)B(j\omega)$ is commonly known as the loop gain. For oscillation to occur, the closed-loop system must have a nonzero output signal with zero input signal.

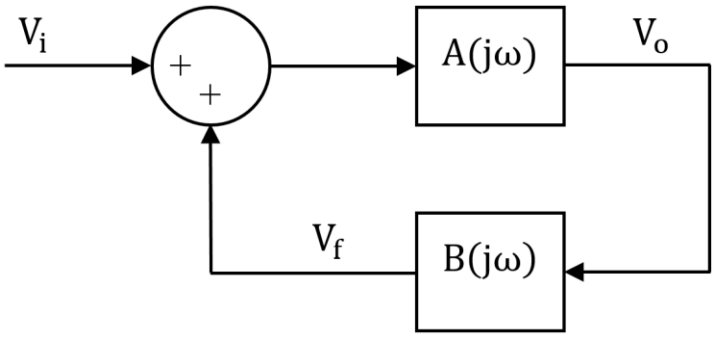

Figure 3.1: A generic oscillator feedback loop.

Consequently, if $V_i = 0$, it follows that the denominator must be zero for a finite V_o to exist. For this condition to be met, the loop gain must be unity. This condition is known as the Barkhausen criterion and is summarized in (3.2) [5].

$$A(j\omega)B(j\omega) = 1 \tag{3.2}$$

Separating (3.2) into real and imaginary parts results in the rectangular form of the Barkhausen criterion. Equations (3.3) and (3.4) summarize this relationship.

$$Re\big(A(j\omega)B(j\omega)\big) = 1 \tag{3.3}$$

$$Im\big(A(j\omega)B(j\omega)\big) = 0 \tag{3.4}$$

For illustrative purposes, the amplifier voltage gain is assumed to be a real constant. This condition is typical of an amplifier working well below its maximum output voltage and bandwidth limitations [5].

$$A(j\omega) = A_{vo} \tag{3.5}$$

The feedback gain is now described as the sum of its real and imaginary parts

$$B(j\omega) = B_r(\omega) + jB_i(\omega). \tag{3.6}$$

Substituting (3.5) and (3.6) into (3.3) and (3.4) results in:

$$A_{vo} = \frac{1}{B_r(\omega)} \tag{3.7}$$

$$B_i(\omega) = 0 \tag{3.8}$$

Equation (3.7) is known as the gain condition [5]. It describes the gain required for the closed-loop system to oscillate, though it does not predict the stability of the oscillation. A separate stability test will be required to determine if the closed-loop system will sustain oscillation for a given amplifier gain. Typically, the amplifier gain will need to be larger than the gain condition in order for oscillation to be self-starting. This means that the gain will need to be adjusted between starting and sustaining oscillation in order to avoid saturating behavior in the amplifier [5]. Automatic gain control can be used to shift the gain dynamically, though it is not pursued here.

Equation (3.8) is known as the frequency of oscillation condition [5]. It predicts the frequency when the phase shift around the closed-loop is 0^o or a multiple of 360^o. Since the system poles cannot be precisely placed on the imaginary axis, the frequency of oscillation will tend to vary as the poles shift. This will cause the output of the oscillator to have a narrow spectrum of frequencies centered around the fundamental frequency. The frequency of oscillation condition can be used to estimate this fundamental frequency.

3.3 Analysis of a Typical Pierce Oscillator

The Barkhausen criterion is now applied to the analysis of a typical Pierce oscillator. Figure 3.2 shows a typical Pierce oscillator based on an op amp [5]. In this circuit, the feedback network of an inverting amplifier is modified by a capacitive voltage divider and inductor.

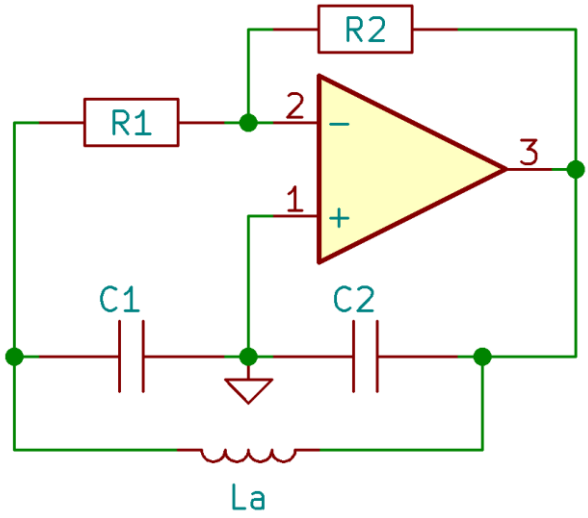

Figure 3.2: Circuit diagram of a typical Pierce oscillator.

If the op amp is well within its operating limits, then the inverting amplifier can be replaced with a voltage-controlled voltage source model [5]. This modification is shown in Figure 3.3.

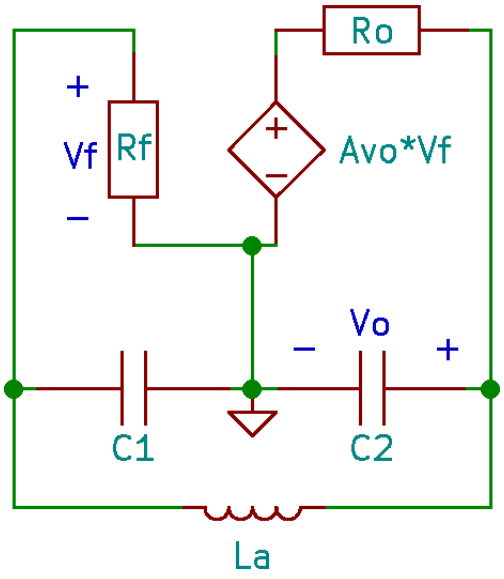

Figure 3.3: Depiction of a typical Pierce oscillator circuit using a voltage-controlled voltage source model for the op amp.

The amplifier gain from Figure 3.3 is defined by (3.9).

$$A_{vo} \triangleq -\frac{R_2}{R_1} \tag{3.9}$$

For convenience, the circuit in Figure 3.3 is rearranged in Figure 3.4.

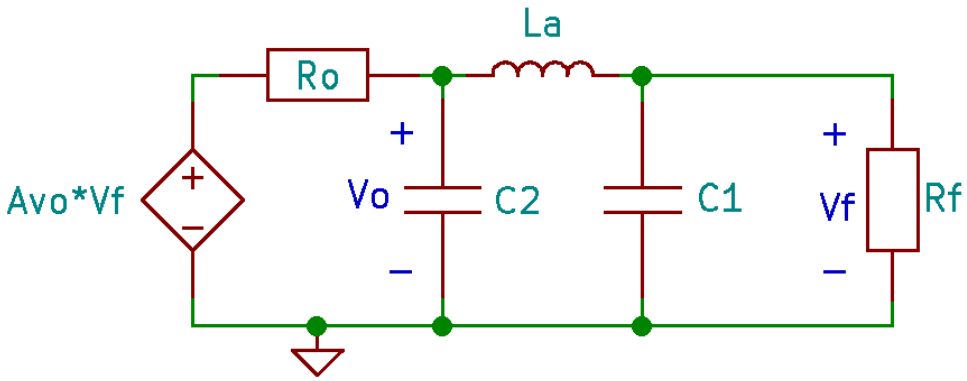

Figure 3.4: Rearranged circuit from Figure 3.3.

The impedance of R_f is typically much greater than the impedance of C_1. Therefore, R_f is treated as an open circuit and excluded from the analysis [5]. Assuming R_f and C_1 are directly in parallel, V_f is redefined as the voltage across C_1.

3.3.1 Barkhausen Criterion

The feedback gain is found by analyzing the circuit elements on the right side of C_2 [5]. These elements are shown in the circuit in Figure 3.5. The feedback gain of the circuit in Figure 3.5 is defined by (3.10) [5].

$$B(j\omega) \triangleq \frac{V_f}{V_o} \tag{3.10}$$

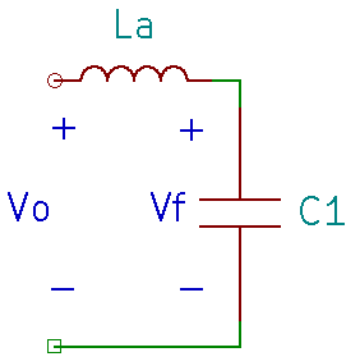

Figure 3.5: Feedback gain elements from Figure 3.4.

The current output from voltage source V_o is found by applying Ohm's law for reactive circuits:

$$I = \frac{V_o}{Z_T} \tag{3.11}$$

where the total impedance of the leg is defined by (3.12).

$$Z_T \triangleq Z_{L_A} + Z_{C_1} \tag{3.12}$$

The voltage across C_1 is found by substituting (3.11) into Ohm's law for C_1.

$$V_{C_1} = IZ_{C_1} = \frac{V_o Z_{C_1}}{Z_T} \tag{3.13}$$

Since the voltage across C_1 is equivalent to V_f, the feedback gain is found by substituting (3.13) into (3.10).

$$B(j\omega) = \frac{V_f}{V_o} = \frac{V_o Z_{C_1}}{V_o Z_T} = \frac{Z_{C_1}}{Z_T} \tag{3.14}$$

The amplifier voltage gain for the circuit in Figure 3.4 is defined by (3.15) [5].

$$A(j\omega) \triangleq \frac{V_o}{V_f} \tag{3.15}$$

The amplifier output current is found through application of Ohm's law for reactive circuits.

$$I_o = \frac{A_{vo}V_f}{R_o + Z_B} \tag{3.16}$$

Where the total feedback network impedance is defined by (3.17).

$$Z_B \triangleq \frac{Z_T Z_{C_2}}{Z_T + Z_{C_2}} \tag{3.17}$$

The output voltage V_o is found by substituting (3.16) into Ohm's law for the total feedback network.

$$V_o = I_o Z_B = \frac{A_{vo}V_f Z_B}{R_o + Z_B} = \frac{A_{vo}V_f}{\frac{R_o}{Z_B} + 1} \tag{3.18}$$

Substituting (3.17) into (3.18) results in:

$$V_o = \frac{A_{vo}V_f}{\frac{R_o(Z_T + Z_{C_2})}{Z_T Z_{C_2}} + 1} \tag{3.19}$$

Rearranging (3.19) results in the amplifier voltage gain. Note that (3.20) collapses to A_{vo} if the output impedance R_o is ideally zero.

$$A(j\omega) = \frac{A_{vo}Z_T Z_{C_2}}{R_o(Z_T + Z_{C_2}) + Z_T Z_{C_2}} \tag{3.20}$$

The loop gain is found by multiplying (3.14) and (3.20).

$$A(j\omega)B(j\omega) = \frac{A_{vo}Z_{C_1} Z_{C_2}}{R_o(Z_T + Z_{C_2}) + Z_T Z_{C_2}} \tag{3.21}$$

It is worth pointing out that the structure of (3.21) will not change if elements are added in series with the inductor. This means that (3.21) can be adapted for use on modified versions of this oscillator, so long as only the impedance Z_T changes. The impedance of each circuit element is

now defined as a function of reactance:

$$Z_{C_1} \triangleq jX_{C_1} \tag{3.22}$$

$$Z_{C_2} \triangleq jX_{C_2} \tag{3.23}$$

$$Z_{L_A} \triangleq jX_{L_A} \tag{3.24}$$

Substituting (3.22)–(3.24) into (3.12) and (3.21) results in (3.25).

$$A(j\omega)B(j\omega) = \frac{A_{vo}j^2X_{C_1}X_{C_2}}{R_oj\left(X_{L_A}+X_{C_1}+X_{C_2}\right)+j^2\left(X_{L_A}+X_{C_1}\right)X_{C_2}} \tag{3.25}$$

Simplification of (3.25) results in (3.26).

$$A(j\omega)B(j\omega) = \frac{A_{vo}X_{C_1}X_{C_2}}{\left(X_{L_A}+X_{C_1}\right)X_{C_2}-jR_o\left(X_{L_A}+X_{C_1}+X_{C_2}\right)} \tag{3.26}$$

The loop gain is separated into its real and imaginary parts.

$$\overline{D} = \left(X_{L_A}+X_{C_1}\right)X_{C_2}+jR_o\left(X_{L_A}+X_{C_1}+X_{C_2}\right) \tag{3.27}$$

$$A(j\omega)B(j\omega) = \frac{A_{vo}X_{C_1}X_{C_2}}{\left(X_{L_A}+X_{C_1}\right)X_{C_2}-jR_o\left(X_{L_A}+X_{C_1}+X_{C_2}\right)} \times \frac{\overline{D}}{\overline{D}} \tag{3.28}$$

Simplification of (3.28) results in the loop gain as a sum of its real and imaginary parts.

$$A(j\omega)B(j\omega) = \frac{A_{vo}X_{C_1}X_{C_2}\left(\left(X_{L_A}+X_{C_1}\right)X_{C_2}+jR_o\left(X_{L_A}+X_{C_1}+X_{C_2}\right)\right)}{\left(\left(X_{L_A}+X_{C_1}\right)X_{C_2}\right)^2+\left(R_o\left(X_{L_A}+X_{C_1}+X_{C_2}\right)\right)^2} \tag{3.29}$$

The imaginary part of (3.29) is set to zero to find the frequency of oscillation condition. This is shown in (3.30).

$$Im\left(A(j\omega)B(j\omega)\right) = \frac{A_{vo}X_{C_1}X_{C_2}\left(R_o\left(X_{L_A}+X_{C_1}+X_{C_2}\right)\right)}{\left(\left(X_{L_A}+X_{C_1}\right)X_{C_2}\right)^2+\left(R_o\left(X_{L_A}+X_{C_1}+X_{C_2}\right)\right)^2} = 0 \tag{3.30}$$

Rearranging (3.30) results in

$$X_{L_A} + X_{C_1} + X_{C_2} = 0. \tag{3.31}$$

The reactances of the circuit elements are now defined as:

$$X_{L_A} \triangleq \omega L_A \tag{3.32}$$

$$X_{C_1} \triangleq \frac{-1}{\omega C_1} \tag{3.33}$$

$$X_{C_2} \triangleq \frac{-1}{\omega C_2} \tag{3.34}$$

Substituting (3.32)–(3.34) into (3.31) results in (3.35).

$$\omega L_A = \frac{1}{\omega C_1} + \frac{1}{\omega C_1} \tag{3.35}$$

Equation (3.35) is rearranged to solve for the frequency of oscillation condition.

$$\omega = \sqrt{\frac{C_1 + C_2}{L_A C_1 C_2}} \tag{3.36}$$

An important feature of this oscillator is illustrated in (3.36). That is to say, the fundamental frequency of this oscillator can be changed by varying the inductance of a single inductor. Additionally, assuming the output of (3.36) is always positive, (3.36) is a strictly monotonic function of L_A. The result of this is that the inductance can be uniquely determined from the fundamental frequency of the oscillator. This is the primary reason why a modified version of this oscillator is discussed for self-sensing.

The real part of (3.29) is set to unity to find the gain condition.

$$Re\big(A(j\omega)B(j\omega)\big) = \frac{A_{vo}X_{C_1}X_{C_2}\left(\left(X_{L_A}+X_{C_1}\right)X_{C_2}\right)}{\left(\left(X_{L_A}+X_{C_1}\right)X_{C_2}\right)^2+\left(R_o\left(X_{L_A}+X_{C_1}+X_{C_2}\right)\right)^2} = 1 \tag{3.37}$$

Rearranging (3.37) and Substituting (3.31) results in

$$A_{vo}X_{C_1}X_{C_2} = \left(\left(X_{L_A}+X_{C_1}\right)X_{C_2}\right). \tag{3.38}$$

Rearranging (3.38) results in

$$A_{vo}X_{C_1} = X_{L_A}+X_{C_1}. \tag{3.39}$$

Equation (3.31) can be rewritten as

$$X_{L_A} = -X_{C_1}-X_{C_2}. \tag{3.40}$$

Substituting (3.40) into (3.39) results in

$$A_{vo}X_{C_1} = -X_{C_2}. \tag{3.41}$$

Substituting (3.9), (3.33), and (3.34) results in the gain condition.

$$\frac{R_2}{R_1} = \frac{C_1}{C_2} \tag{3.42}$$

3.3.2 Stability Analysis

If the transient response of the op amp can be ignored, then the state space dynamics of the typical Pierce oscillator are described by (3.43).

$$\dot{X} = FX \Rightarrow \begin{bmatrix}\dot{V}_{C_1}\\ \ddot{V}_{C_1}\\ \dot{V}_{C_2}\end{bmatrix} = \begin{bmatrix}0 & 1 & 0\\ \dfrac{-1}{L_AC_1} & 0 & \dfrac{1}{L_AC_1}\\ \dfrac{A_{vo}}{R_oC_2} & -\dfrac{C_1}{C_2} & \dfrac{-1}{R_oC_2}\end{bmatrix}\begin{bmatrix}V_{C_1}\\ \dot{V}_{C_1}\\ V_{C_2}\end{bmatrix} \tag{3.43}$$

The characteristic equation for this system is defined by

$$P(s) \triangleq det(sI - F). \tag{3.44}$$

Substituting (3.43) into (3.44) results in (3.45).

$$P(s) = s^3 + \left(\frac{1}{R_o C_2}\right)s^2 + \left(\frac{C_1 + C_2}{L_A C_1 C_2}\right)s + \left(\frac{1 - A_{vo}}{R_o L_A C_1 C_2}\right) \tag{3.45}$$

Two factors are defined for convenience.

$$\omega_f^2 \triangleq \frac{C_1 + C_2}{L_A C_1 C_2} \tag{3.46}$$

$$\tau \triangleq R_o C_2 \tag{3.47}$$

The characteristic equation is now rewritten by substituting (3.46) and (3.47) into (3.45).

$$P(s) = s^3 + \left(\frac{1}{\tau}\right)s^2 + \left(\omega_f^2\right)s + \left(\frac{1 - A_{vo}}{\tau L_A C_1}\right) \tag{3.48}$$

The roots of (3.48) represent the eigenvalues of this autonomous system. Instead of finding the roots directly, the stability of the system is analyzed with the Routh-Hurwitz stability criterion [6]. Equation (3.49) shows the completed Routh array for this system

$$\begin{array}{ccc} s^3 & 1 & \omega_f^2 \\ s^2 & \frac{1}{\tau} & \frac{1 - A_{vo}}{\tau L_A C_1} \\ s & b_1 & 0 \\ 1 & b_2 & 0 \end{array} \tag{3.49}$$

where b_1 is defined by (3.50) and b_2 is defined by (3.51).

$$b_1 \triangleq \frac{-(1)\left(\frac{1 - A_{vo}}{\tau L_A C_1}\right) + \left(\frac{1}{\tau}\right)\left(\omega_f^2\right)}{\frac{1}{\tau}} = \frac{1}{L_A C_1}\left(\frac{C_1}{C_2} + A_{vo}\right) \tag{3.50}$$

$$b_2 \triangleq \frac{-\left(\frac{1}{\tau}\right)(0) + \left(\frac{1 - A_{vo}}{\tau L_A C_1}\right)(b_1)}{b_1} = \frac{1}{L_A C_1}\left(\frac{1 - A_{vo}}{R_o C_2}\right) \tag{3.51}$$

The first column of the Routh array must have all positive elements for the system to be stable [6]. Since τ is positive by definition, only the inequalities in (3.52) and (3.53) need to be satisfied for stability.

$$\frac{1}{L_A C_1}\left(\frac{C_1}{C_2} + A_{vo}\right) > 0 \tag{3.52}$$

$$\frac{1}{L_A C_1}\left(\frac{1 - A_{vo}}{R_o C_2}\right) > 0 \tag{3.53}$$

Equations (3.52) and (3.53) simplify to:

$$\frac{C_1}{C_2} > \frac{R_2}{R_1} \tag{3.54}$$

$$1 + \frac{R_2}{R_1} > 0 \tag{3.55}$$

The left-hand side of (3.55) is greater than zero by definition. Therefore, the deciding factor for stability of the closed-loop system is (3.54). Since self-sustained oscillation is the desired behavior of the oscillator, the inverse of (3.54) can be used as a design requirement for the oscillator. This is combined with the gain condition in (3.42) to yield the gain design constraint for this oscillator.

$$\frac{R_2}{R_1} \geq \frac{C_1}{C_2} \tag{3.56}$$

3.4 Modified Pierce Oscillator

The Barkhausen criterion is now applied to the modified Pierce oscillator shown in Figure 3.6. The fixed inductor in the typical Pierce oscillator is replaced with the electrical model of a PIVI voice-

coil actuator. A current source, I_A, is added to simulate a power source for driving the actuator. Capacitors C_{b1} and C_{b2} are added to DC isolate the op amp from both the actuator and current source.

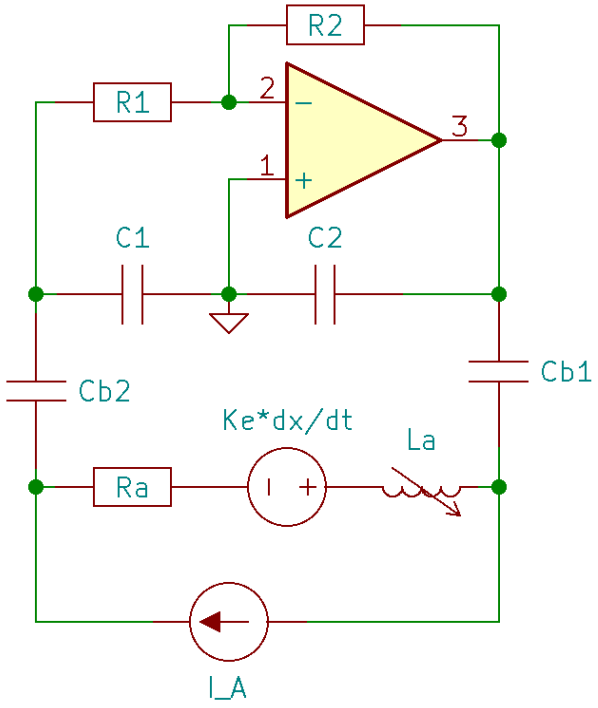

Figure 3.6: Circuit diagram of a modified Pierce oscillator.

3.4.1 Simplifying Assumptions

Two main assumptions are made to simplify the analysis of the modified Pierce oscillator. First, the maximum operating frequency of the actuator and current source, $F_{A\,Max}$, is assumed to be much lower than the lowest fundamental frequency of the oscillator $F_{O\,Min}$. In other words, the motion of the actuator is slow enough that the back emf can be treated as DC on the time scale of the oscillator's lowest fundamental frequency. The same also goes for the current source. That is

to say, the current output is at a low enough frequency to be considered DC on the time scale of the oscillator's lowest fundamental frequency. Due to the impedance of capacitors C_{b1} and C_{b2}, the low-frequency back emf and current source signals will be attenuated relative to the oscillator feedback signal. Therefore, the back emf and the signal output of the current source can be ignored in this analysis. The result of this assumption is that the frequency-bands of the actuator and oscillator are separated by a buffer band. The size of this buffer band, shown in Figure 3.7, is chosen to ensure that the low-frequency assumption is valid.

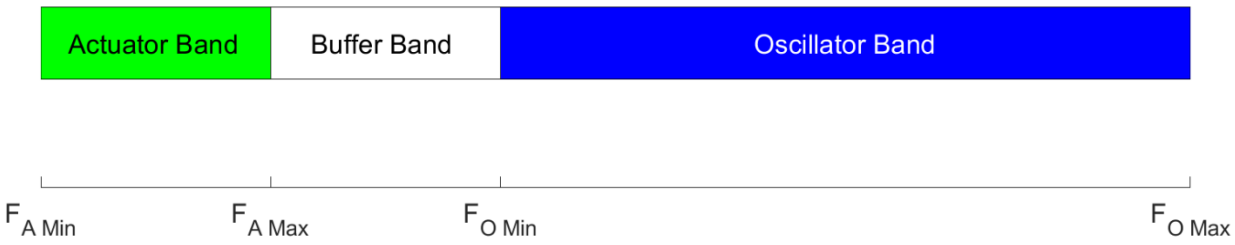

Figure 3.7: Depiction of the actuator and oscillator frequency-bands. Frequencies $F_{A\,Max}$ and $F_{O\,Min}$ are chosen such that the buffer band sufficiently separates the two frequency-bands. This separation ensures that the impedances of capacitors C_{b1} and C_{b2} are much higher at $F_{A\,Max}$ than at $F_{O\,Min}$.

Second, the impedance of the current source is assumed to be practically infinite. So, it is assumed to be an open circuit and is removed from the model. The validity of this assumption will be revisited when parasitic capacitance from the current source is considered. The result of these two assumptions is that, in this modified circuit, the PIVI actuator behaves as a variable inductor with series winding resistance. This is shown in Figure 3.8.

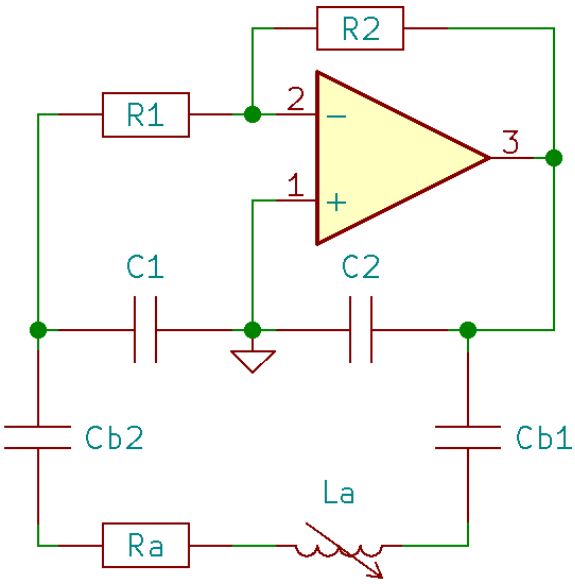

Figure 3.8: Simplified circuit model of the modified Pierce oscillator.

3.4.2 Barkhausen Criterion

The circuit in Figure 3.8 is modeled in the same manner as the typical Pierce oscillator by replacing the op amp with a voltage-controlled voltage source. The updated circuit model is shown in Figure 3.9. Note that, again, the input impedance is assumed to be very large, so it is neglected in this analysis. The amplifier gain was defined previously in (3.9). Repeated here for convenience:

$$A_{vo} \triangleq -\frac{R_2}{R_1} \tag{3.9}$$

If the circuit in Figure 3.9 is compared with the circuit in Figure 3.4, it can be seen that the modified Pierce oscillator circuit only differs by the elements in series with the inductor.

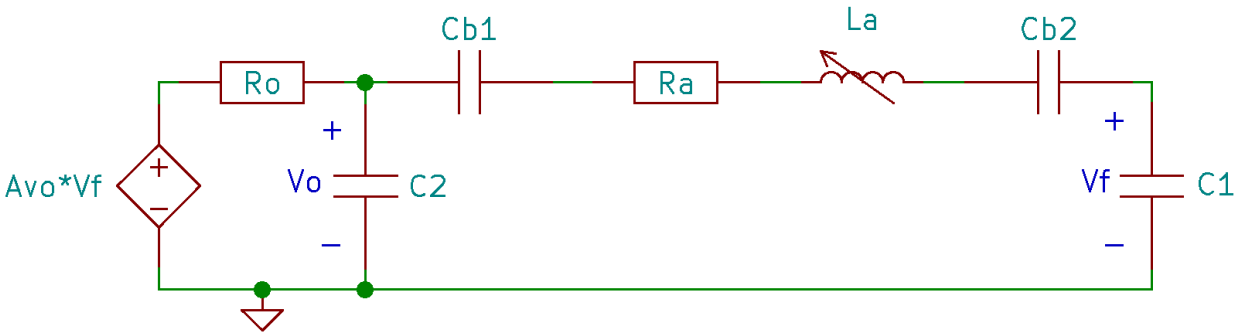

Figure 3.9: Updated circuit model of the modified Pierce oscillator. The op amp is replaced with a voltage-controlled voltage source model, and the circuit diagram is rearranged for clarity.

Therefore, the loop gain of the typical Pierce oscillator can be reused for the modified Pierce oscillator. Equation (3.21) is repeated here for convenience.

$$A(j\omega)B(j\omega) = \frac{A_{vo}Z_{C_1}Z_{C_2}}{R_o\left(Z_T + Z_{C_2}\right) + Z_T Z_{C_2}} \tag{3.21}$$

Z_T is redefined for the modified circuit. In the same manner as before, it is defined as the total impedance for the right half of the feedback network:

$$Z_T \triangleq Z_{L_A} + Z_{C_1} + Z_{C_{b1}} + Z_{C_{b2}} \tag{3.57}$$

The impedance of each circuit element is now defined as a function of reactance and resistance.

$$Z_{L_A} \triangleq R_A + jX_{L_A} \tag{3.58}$$

$$Z_{C_1} \triangleq jX_{C_1} \tag{3.59}$$

$$Z_{C_2} \triangleq jX_{C_2} \tag{3.60}$$

$$Z_{C_{b1}} \triangleq jX_{C_{b1}} \tag{3.61}$$

$$Z_{C_{b2}} \triangleq jX_{C_{b2}} \tag{3.62}$$

Substituting (3.57)–(3.62) into (3.21) results in (3.63).

$$A(j\omega)B(j\omega) = G_L = \frac{j^2 A_{vo} X_{C_1} X_{C_2}}{R_o\left(R_A + j\left(X_{L_A} + X_{C_1} + X_{C_2} + X_{C_{b1}} + X_{C_{b2}}\right)\right) + \left(R_A + j\left(X_{L_A} + X_{C_1} + X_{C_{b1}} + X_{C_{b2}}\right)\right) j X_{C_2}} \tag{3.63}$$

The term G_L is now defined as the loop gain and (3.63) is separated into its real and imaginary components.

$$G_L = \frac{-A_{vo} X_{C_1} X_{C_2}\left(\left(R_o R_A - \left(X_{L_A} + X_{C_1} + X_{C_{b1}} + X_{C_{b2}}\right) X_{C_2}\right) - j\left(R_A X_{C_2} + R_o\left(X_{L_A} + X_{C_1} + X_{C_2} + X_{C_{b1}} + X_{C_{b2}}\right)\right)\right)}{\left(R_o R_A - \left(X_{L_A} + X_{C_1} + X_{C_{b1}} + X_{C_{b2}}\right) X_{C_2}\right)^2 + \left(R_A X_{C_2} + R_o\left(X_{L_A} + X_{C_1} + X_{C_2} + X_{C_{b1}} + X_{C_{b2}}\right)\right)^2} \tag{3.64}$$

The imaginary part of (3.64) is set to zero to solve for the frequency of oscillation condition.

$$Im(G_L) = \frac{A_{vo} X_{C_1} X_{C_2}\left(R_A X_{C_2} + R_o\left(X_{L_A} + X_{C_1} + X_{C_2} + X_{C_{b1}} + X_{C_{b2}}\right)\right)}{\left(R_o R_A - \left(X_{L_A} + X_{C_1} + X_{C_{b1}} + X_{C_{b2}}\right) X_{C_2}\right)^2 + \left(R_A X_{C_2} + R_o\left(X_{L_A} + X_{C_1} + X_{C_2} + X_{C_{b1}} + X_{C_{b2}}\right)\right)^2} = 0 \tag{3.65}$$

Simplifying (3.65) results in

$$R_A X_{C_2} + R_o\left(X_{L_A} + X_{C_1} + X_{C_2} + X_{C_{b1}} + X_{C_{b2}}\right) = 0. \tag{3.66}$$

The reactances of the circuit elements are now defined as:

$$X_{L_A} = \omega L_A \tag{3.67}$$

$$X_{C_1} \triangleq \frac{-1}{\omega C_1} \tag{3.68}$$

$$X_{C_2} \triangleq \frac{-1}{\omega C_2} \tag{3.69}$$

$$X_{C_{b1}} \triangleq \frac{-1}{\omega C_{b1}} \tag{3.70}$$

$$X_{C_{b2}} \triangleq \frac{-1}{\omega C_{b2}} \tag{3.71}$$

Substituting (3.67)–(3.71) into (3.66) results in (3.72).

$$-\frac{R_A}{\omega C_2}+R_o\left(\omega L_A-\frac{1}{\omega}\left(\frac{1}{C_1}+\frac{1}{C_2}+\frac{1}{C_{b1}}+\frac{1}{C_{b2}}\right)\right)=0 \tag{3.72}$$

Solving (3.72) for the frequency yields (3.73).

$$\omega=\sqrt{\frac{R_A}{R_o L_A C_2}+\frac{1}{L_A C_T}} \tag{3.73}$$

where the total capacitance is defined by (3.74).

$$C_T \triangleq \left(\frac{1}{C_1}+\frac{1}{C_2}+\frac{1}{C_{b1}}+\frac{1}{C_{b2}}\right)^{-1}=\frac{C_1C_2C_{b1}C_{b2}}{C_1C_2C_{b1}+C_1C_2C_{b2}+C_1C_{b1}C_{b2}+C_2C_{b1}C_{b2}} \tag{3.74}$$

Equation (3.73) shows that this modified circuit behaves in a similar manner to the typical Pierce oscillator. That is to say, the fundamental frequency of the modified circuit can be changed by varying the inductance of a single inductor. Additionally, assuming the output of (3.73) is always positive, (3.73) is a strictly monotonic function of L_A. However, in this case, a PIVI actuator serves as the inductor in the circuit. Therefore, since the inductance of a PIVI actuator is defined to be a strictly monotonic function of the position, the fundamental frequency of the modified circuit is also a strictly monotonic function of the position. The result of this is that the position of the actuator can be uniquely determined from the fundamental frequency of this modified Pierce oscillator.

The real part of (3.64) is set to unity to solve for the gain condition.

$$Re(G_L)=\frac{-A_{vo}X_{C_1}X_{C_2}\left(R_oR_A-\left(X_{L_A}+X_{C_1}+X_{C_{b1}}+X_{C_{b2}}\right)X_{C_2}\right)}{\left(R_oR_A-\left(X_{L_A}+X_{C_1}+X_{C_{b1}}+X_{C_{b2}}\right)\right)^2+\left(R_AX_{C_2}+R_o\left(X_{L_A}+X_{C_1}+X_{C_2}+X_{C_{b1}}+X_{C_{b2}}\right)\right)^2}=1 \tag{3.75}$$

Substituting (3.66) into (3.75) results in (3.76).

$$A_{vo}X_{C_1}X_{C_2} = -R_oR_A + \left(X_{L_A} + X_{C_1} + X_{C_{b1}} + X_{C_{b2}}\right)X_{C_2} \tag{3.76}$$

Rearranging and substituting (3.67)–(3.71) into (3.76) results in

$$A_{vo} = -\omega^2 R_o R_A C_1 C_2 \; - \omega C_1 \left(\omega L_A - \frac{1}{\omega}\left(\frac{1}{C_1} + \frac{1}{C_{b1}} + \frac{1}{C_{b2}}\right)\right). \tag{3.77}$$

Rearranging (3.77) results in

$$A_{vo} = -\omega^2 C_1 (R_o R_A C_2 + L_A) + C_1 \left(\frac{1}{C_1} + \frac{1}{C_{b1}} + \frac{1}{C_{b2}}\right). \tag{3.78}$$

Substituting (3.73) and (3.74) into (3.78) yields

$$A_{vo} = -\left(\frac{R_A C_T + R_o C_2}{R_o L_A C_2 C_T}\right) C_1 (R_o R_A C_2 + L_A) + C_1 \left(\frac{1}{C_T} - \frac{1}{C_2}\right). \tag{3.79}$$

Simplifying and substituting (3.9) into (3.79) results in the gain condition.

$$\frac{R_2}{R_1} = C_1 R_A \left(\frac{R_A}{L_A} + \frac{1}{R_o C_2} + \frac{R_o C_2}{L_A C_T}\right) + \frac{C_1}{C_2} \tag{3.80}$$

3.4.3 Stability Analysis

Ignoring the transient behavior of the op amp, the state space dynamics of the modified circuit are described by (3.81).

$$\dot{X} = FX \Rightarrow \begin{bmatrix} \dot{V}_{C_1} \\ \dot{V}_{C_2} \\ \dot{V}_{C_{b1}} \\ \dot{V}_{C_{b1}} \\ \dot{I}_A \end{bmatrix} = \begin{bmatrix} 0 & 0 & 0 & 0 & \frac{1}{C_1} \\ \frac{A_{vo}}{R_o C_2} & \frac{-1}{R_o C_2} & 0 & 0 & \frac{-1}{C_2} \\ 0 & 0 & 0 & 0 & \frac{1}{C_{b_1}} \\ 0 & 0 & 0 & 0 & \frac{1}{C_{b_2}} \\ \frac{-1}{L_A} & \frac{1}{L_A} & \frac{-1}{L_A} & \frac{-1}{L_A} & \frac{-R_A}{L_A} \end{bmatrix} \begin{bmatrix} V_{C_1} \\ V_{C_2} \\ V_{C_{b1}} \\ V_{C_{b2}} \\ I_A \end{bmatrix} \tag{3.81}$$

The characteristic equation for this system is defined by (3.44). Restated here for convenience

$$P(s) \triangleq det(sI - F). \tag{3.44}$$

Substituting (3.81) into (3.44) results in (3.82).

$$P(s) = s^5 + \left(\frac{1}{R_o C_2} + \frac{R_A}{L_A}\right)s^4 + \left(\frac{R_A}{L_A R_o C_2} + \frac{1}{L_A C_T}\right)s^3 + \left(\frac{C_{b_1}+C_{b_2}}{C_{b_1}C_{b_2}} + \frac{1-A_{vo}}{C_1}\right)\frac{1}{L_A R_o C_2}s^2 \tag{3.82}$$

The two zero roots of the characteristic equation are factored out and the reduced order characteristic equation is used to form the Routh array in (3.83).

$$\begin{array}{lll} s^3 & 1 & \left(\frac{R_A}{L_A R_o C_2} + \frac{1}{L_A C_T}\right) \\ s^2 & \left(\frac{1}{R_o C_2} + \frac{R_A}{L_A}\right) & \left(\frac{C_{b_1}+C_{b_2}}{C_{b_1}C_{b_2}} + \frac{1-A_{vo}}{C_1}\right)\frac{1}{L_A R_o C_2} \\ s & b_1 & 0 \\ 1 & b_2 & 0 \end{array} \tag{3.83}$$

Where:

$$b_1 \triangleq \frac{-(1)\left(\frac{C_{b_1}+C_{b_2}}{C_{b_1}C_{b_2}} + \frac{1-A_{vo}}{C_1}\right)\frac{1}{L_A R_o C_2} + \left(\frac{R_A}{L_A R_o C_2} + \frac{1}{L_A C_T}\right)\left(\frac{1}{R_o C_2} + \frac{R_A}{L_A}\right)}{\left(\frac{1}{R_o C_2} + \frac{R_A}{L_A}\right)} \tag{3.84}$$

$$b_2 \triangleq \frac{-(0)\left(\frac{1}{R_o C_2} + \frac{R_A}{L_A}\right) + (b_1)\left(\frac{C_{b_1}+C_{b_2}}{C_{b_1}C_{b_2}} + \frac{1-A_{vo}}{C_1}\right)\frac{1}{L_A R_o C_2}}{b_1} \tag{3.85}$$

The first two elements of the Routh array are positive by definition, so (3.86) and (3.87) are the only inequalities that must be satisfied for stability.

$$-(1)\left(\frac{C_{b_1}+C_{b_2}}{C_{b_1}C_{b_2}} + \frac{1-A_{vo}}{C_1}\right)\frac{1}{L_A R_o C_2} + \left(\frac{R_A}{L_A R_o C_2} + \frac{1}{L_A C_T}\right)\left(\frac{1}{R_o C_2} + \frac{R_A}{L_A}\right) > 0 \tag{3.86}$$

$$\left(\frac{C_{b_1}+C_{b_2}}{C_{b_1}C_{b_2}} + \frac{1-A_{vo}}{C_1}\right) > 0 \tag{3.87}$$

Substituting (3.9) and simplifying (3.87) results in (3.88).

$$1 + \frac{R_2}{R_1} > -C_1 \frac{C_{b_1} + C_{b_2}}{C_{b_1} C_{b_2}} \tag{3.88}$$

The inequality in (3.88) is true by definition, so the deciding factor for stability is (3.86). Rearranging (3.86) results in

$$C_1 R_A \left(\frac{R_A}{L_A} + \frac{1}{R_o C_2} + \frac{R_o C_2}{L_A C_T} \right) + \frac{C_1}{C_T} > C_1 \left(\frac{1}{C_{b_1}} + \frac{1}{C_{b_2}} \right) + 1 - A_{vo}. \tag{3.89}$$

Substituting (3.74) and (3.9) into (3.89) results in (3.90).

$$C_1 R_A \left(\frac{R_A}{L_A} + \frac{1}{R_o C_2} + \frac{R_o C_2}{L_A C_T} \right) + \frac{C_1}{C_2} > \frac{R_2}{R_1} \tag{3.90}$$

Equation (3.90) is the deciding factor for stability, so the inverse of this equation is used as a design requirement for the oscillator to sustain oscillation. Combining (3.80) and (3.90) yields the gain design constraint for this oscillator.

$$\frac{R_2}{R_1} \geq C_1 R_A \left(\frac{R_A}{L_A} + \frac{1}{R_o C_2} + \frac{R_o C_2}{L_A C_T} \right) + \frac{C_1}{C_2} \tag{3.91}$$

3.5 Parasitic Capacitance

In reality, most high-power current sources have non-negligible parasitic capacitance in parallel with their output terminals. This is shown in the modified Pierce oscillator in Figure 3.10. At high frequencies, this parasitic capacitance violates the high-impedance assumption for the current source. Therefore, the impedance of the current source will have a non-negligible effect on the fundamental frequency of the modified Pierce oscillator. Additionally, although it is assumed to be bounded, the parasitic capacitance need not be constant. This means that the strictly monotonic relationship between the modified Pierce oscillator's fundamental frequency and actuator position

cannot be guaranteed.

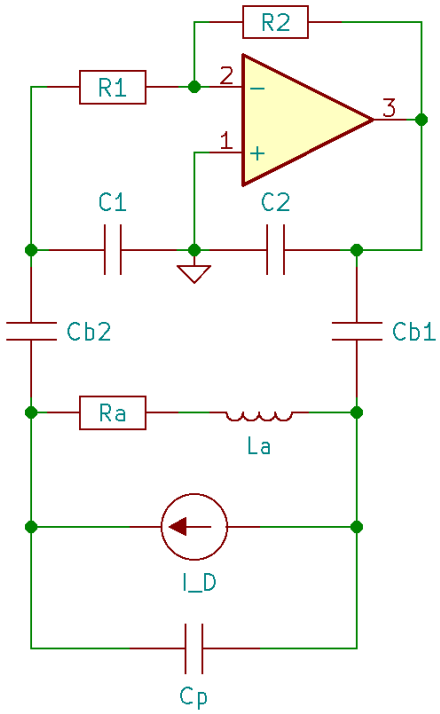

Figure 3.10: Circuit diagram of the modified Pierce oscillator with parasitic capacitance from the current source.

3.5.1 Mitigating Parasitic Capacitance

The effect of the parasitic capacitance can be mitigated if the impedance of the current source is modified. It can be seen Figure 3.10 that the current source is in parallel with the variable inductor and series resistance. If the impedance of the current source is increased well above the impedance of the inductor, then it can be treated as an open circuit, and the effect of the parasitic capacitance will be negligible. This increase in impedance need only occur within the expected band of oscillation frequencies, so it should be possible to compensate for the parasitic capacitance with

the addition of passive components. To this end, further modifications are made to the modified Pierce oscillator. Shown in Figure 3.11, inductor L_q with series resistance R_q and capacitor C_q are used to modify the impedance of the current source.

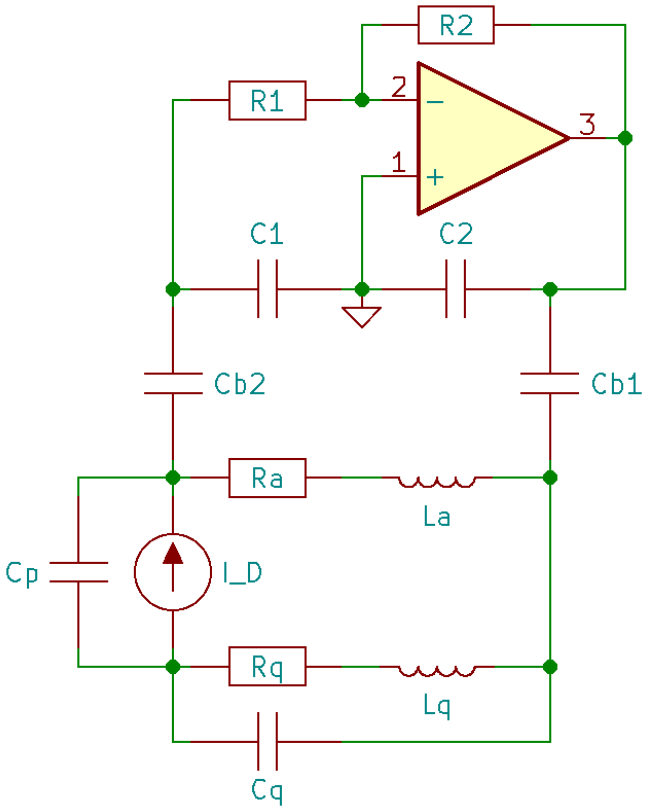

Figure 3.11: Circuit diagram of the modified Pierce oscillator with a compensated current source.

Analysis of this circuit with the Barkhausen Criterion is not trivial due to the possibility of multiple fundamental frequencies. Instead, the impedance of the compensated current source is analyzed. Figure 3.12 shows the isolated components of the current source. Note that the DC impedance of the current source is still considered to be practically infinite, so only the parasitic capacitance is considered.

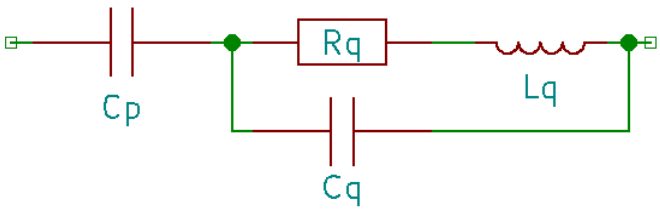

Figure 3.12: Isolated components of the compensated current source.

The impedance of the compensated current source is defined by (3.92).

$$Z_{TP} \triangleq Z_{C_p} + \left(\frac{1}{Z_{C_q}} + \frac{1}{Z_{L_q}}\right)^{-1} \tag{3.92}$$

Rearranging (3.92) results in (3.93).

$$Z_{TP} = Z_{C_p} + \frac{Z_{L_q} Z_{C_q}}{Z_{L_q} + Z_{C_q}} = \frac{Z_{C_p}\left(Z_{L_q} + Z_{C_q}\right) + Z_{L_q} Z_{C_q}}{Z_{L_q} + Z_{C_q}} \tag{3.93}$$

The impedance of each component is now defined:

$$Z_{C_p} \triangleq \frac{1}{j\omega C_p} \tag{3.94}$$

$$Z_{C_q} \triangleq \frac{1}{j\omega C_q} \tag{3.95}$$

$$Z_{L_q} \triangleq R_q + j\omega L_q \tag{3.96}$$

Substituting (3.94)–(3.96) into (3.93) results in the total impedance of the compensated current source.

$$Z_{TP} = \frac{\frac{1}{j\omega C_p}\left(R_q + j\omega L_q + \frac{1}{j\omega C_q}\right) + \left(R_q + j\omega L_q\right)\frac{1}{j\omega C_q}}{R_q + j\omega L_q + \frac{1}{j\omega C_q}} \tag{3.97}$$

Equation (3.97) is rearranged into standard Bode form [6].

$$Z_{TP} = K_0(j\omega)^{-1}\frac{\left(\frac{j\omega}{\omega_z}\right)^2 + 2\zeta_z\left(\frac{j\omega}{\omega_z}\right) + 1}{\left(\frac{j\omega}{\omega_p}\right)^2 + 2\zeta_p\left(\frac{j\omega}{\omega_p}\right) + 1} \tag{3.98}$$

Where:

$$K_0 \triangleq \frac{1}{C_p} \tag{3.99}$$

$$\omega_z^2 \triangleq \frac{1}{L_q(C_p + C_q)} \tag{3.100}$$

$$\zeta_z \triangleq \frac{R_q(C_p + C_q)}{2\sqrt{L_q(C_p + C_q)}} \tag{3.101}$$

$$\omega_p^2 \triangleq \frac{1}{L_q C_q} \tag{3.102}$$

$$\zeta_p \triangleq \frac{R_q C_q}{2\sqrt{L_q C_q}} \tag{3.103}$$

Equation (3.98) shows that the total impedance of the compensated circuit contains a pole at DC, complex-conjugate zeros at corner frequency ω_z, and complex-conjugate poles at corner frequency ω_p. Damping ratios ζ_z and ζ_p control the peak magnitude and bandwidth at the complex-conjugate zeros and poles. A normalized magnitude plot of the total impedance and the parasitic capacitance is shown in Figure 3.13.

In the region between ω_z and ω_p, the magnitude of the total impedance is increased significantly above that of the parasitic capacitance alone. If the oscillator frequency-band is placed within this

region, then, depending on the selection of components L_q and C_q, it should be possible to increase the impedance of the current source well above that of the actuator's variable-inductance. In this case, as discussed previously, the effect of the parasitic capacitance on the fundamental frequency of the oscillator will be reduced significantly. Therefore, this compensation circuit can be used to mitigate parasitic capacitance in a non-ideal current source.

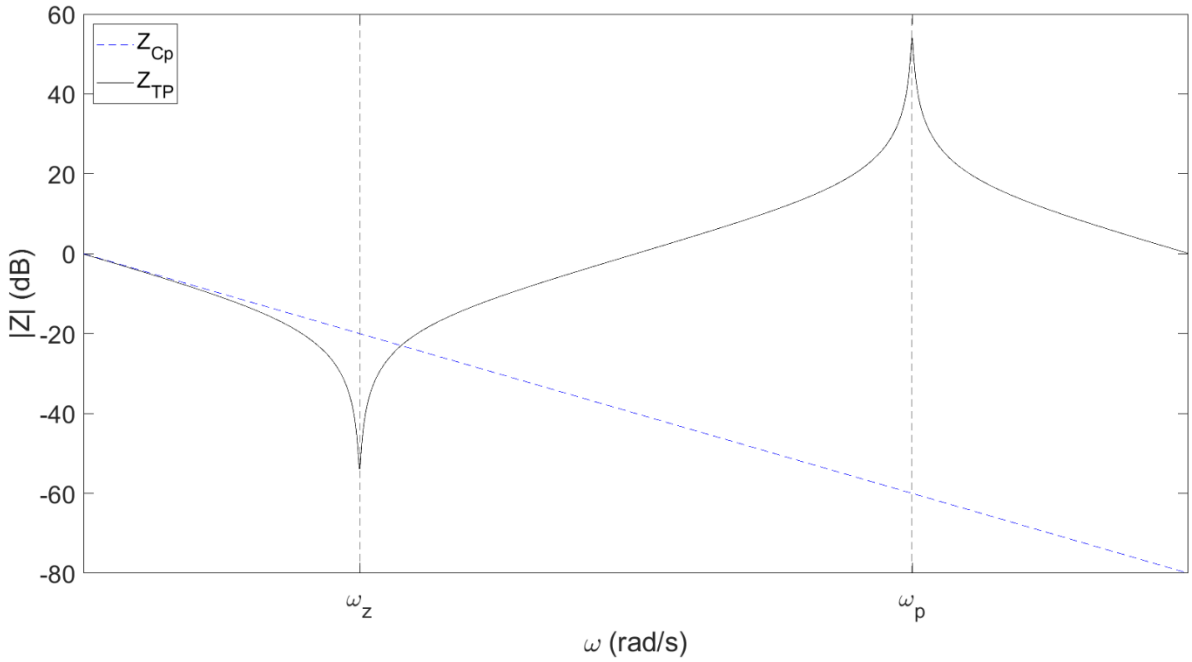

Figure 3.13: Comparison of the normalized magnitude of impedance of the compensated current source and the parasitic capacitance alone. The parasitic capacitance is shown in blue. The compensated current source is shown in black. A damping ratio of 0.01 is used for both second-order terms.

While the increase in impedance afforded by this compensation circuit is desirable, two important caveats should be considered. First, at excitation frequencies near ω_z, the impedance decreases significantly. This behavior can be detrimental to the performance of either the current source or

the oscillator. Therefore, the selection of L_q and C_q should be done in a manner that places the complex-conjugate zeros within the buffer band between the actuator and oscillator frequency-bands. Second, variation in parasitic capacitance will shift the overall impedance of the compensated current source. This can be seen in (3.99)–(3.101), where the location of the DC pole, the location of the second-order zero, and the damping ratio of the second order zero are all dependent on the parasitic capacitance. It is assumed that variations in parasitic capacitance are bounded. Therefore, the selection of L_q and C_q should also be based on the worst case parasitic capacitance within expected bounds.

4. EXPERIMENTAL VALIDATION OF THE MODIFIED PIERCE OSCILLATOR

4.1 Section Overview

In the previous section, a modified Pierce oscillator was analyzed for use in a self-sensing application. In this section, an implementation of the modified Pierce oscillator is presented. A test procedure for this circuit, used to simulate the conditions of a powered PIVI actuator, is then discussed. The results of this test procedure are then presented along with a brief discussion of practical limitations for this self-sensing methodology.

4.2 Experimental Apparatus

Figure 4.1 shows an overview of the circuit used to implement and test the performance of the modified Pierce oscillator. In this circuit, the current source is implemented with a push-pull transconductance amplifier. The circuit implementation itself is shown in Figure 4.2. Note that the transconductance amplifier and modified Pierce oscillator are placed on the same circuit board for manufacturing convenience. Three separate power supplies are used in the test circuit to reduce capacitive coupling between the oscillator and transconductance amplifier stages. This power supply arrangement is shown in Figure 4.3.

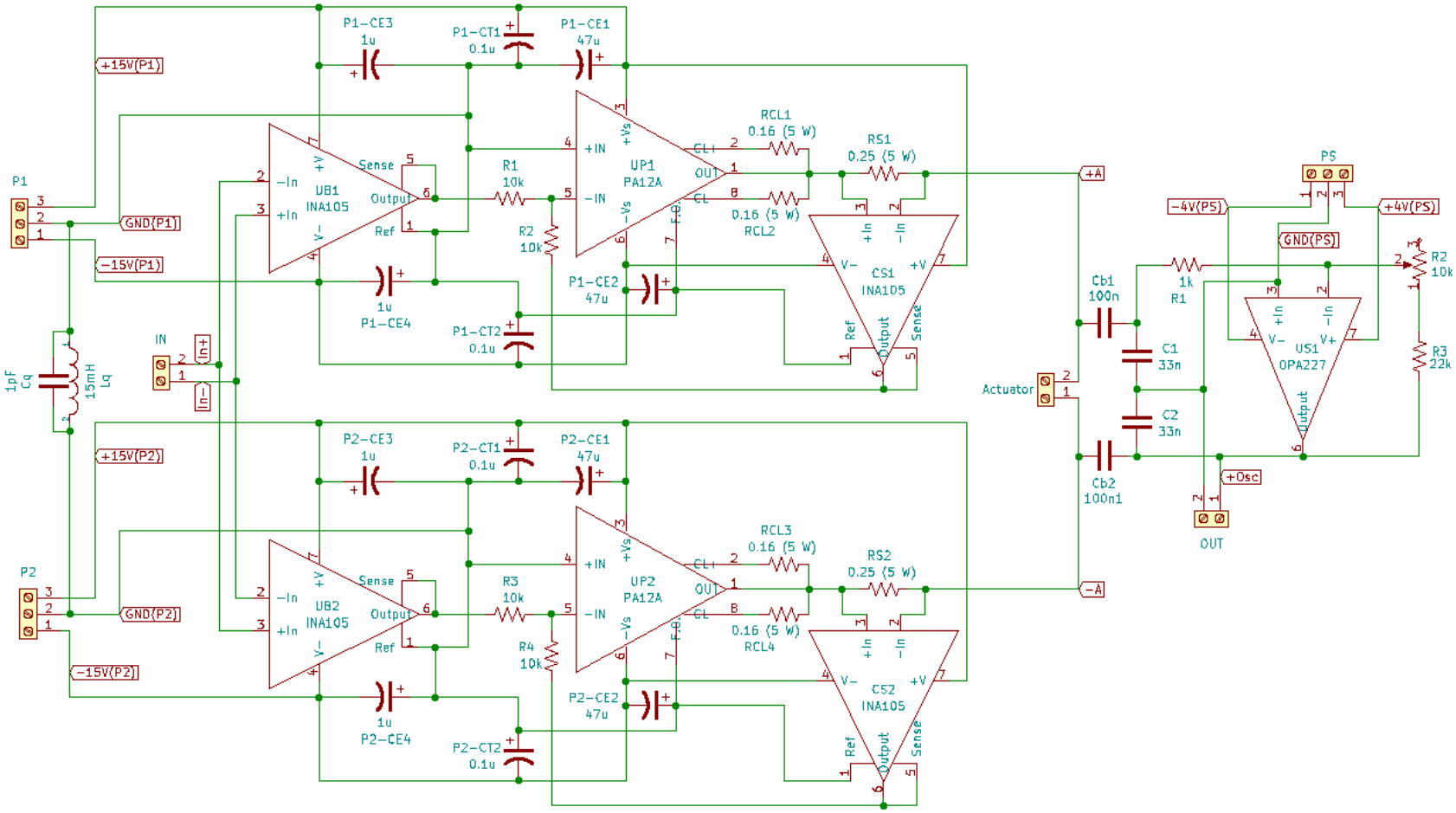

Figure 4.1: Diagram of the test circuit. The modified Pierce oscillator is on the right side of the diagram. The current source, implemented as a transconductance amplifier, is on the left side of the diagram. Power supplies P1, P2, and PS do not share common rails or a common ground.

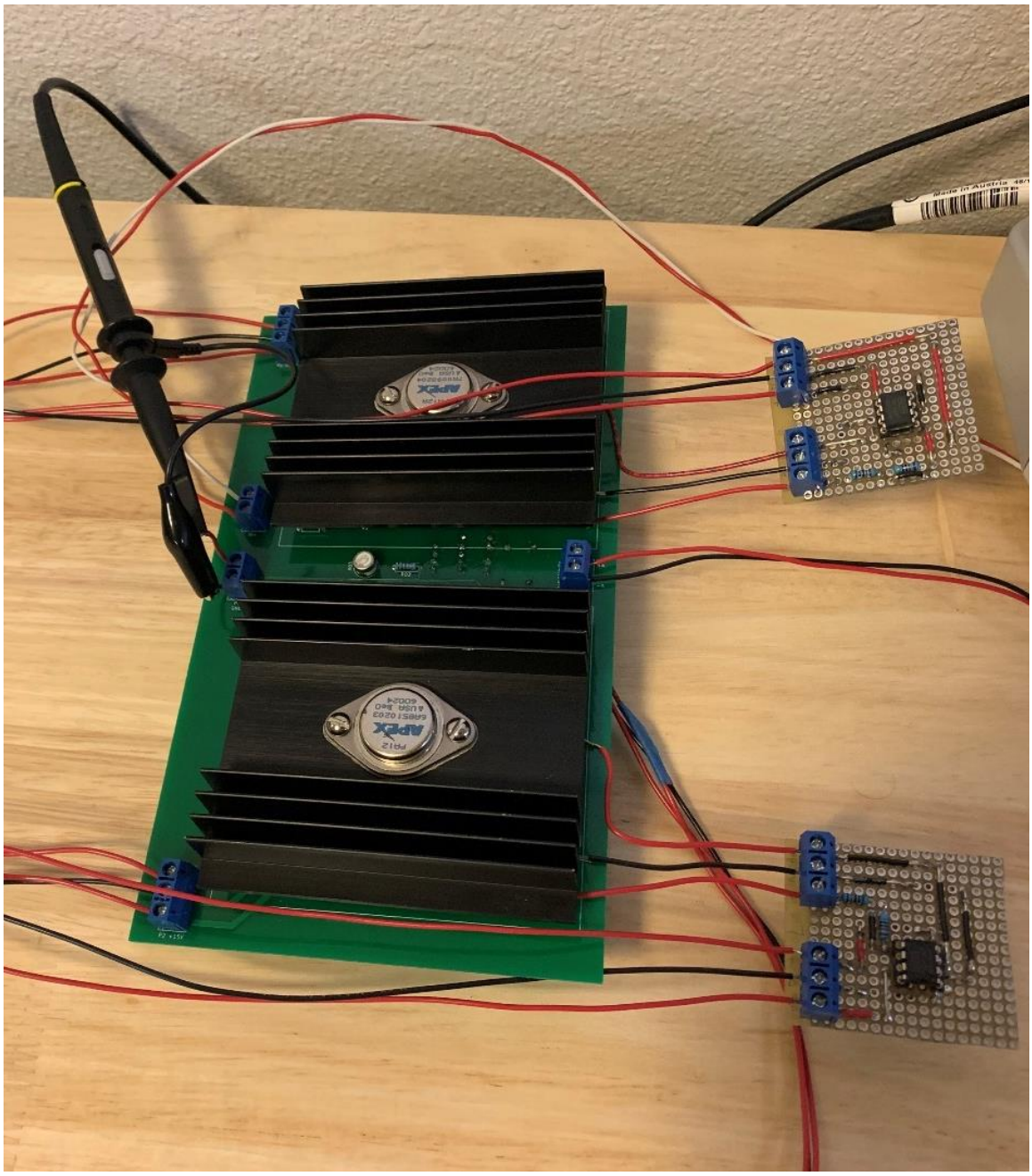

Figure 4.2: Implementation of the test circuit in Figure 4.1. The protoboards on the right-hand side of the picture are current sense amplifiers used for the transconductance amplifier stages. These elements were placed on separate boards because they were neglected in the original circuit design.

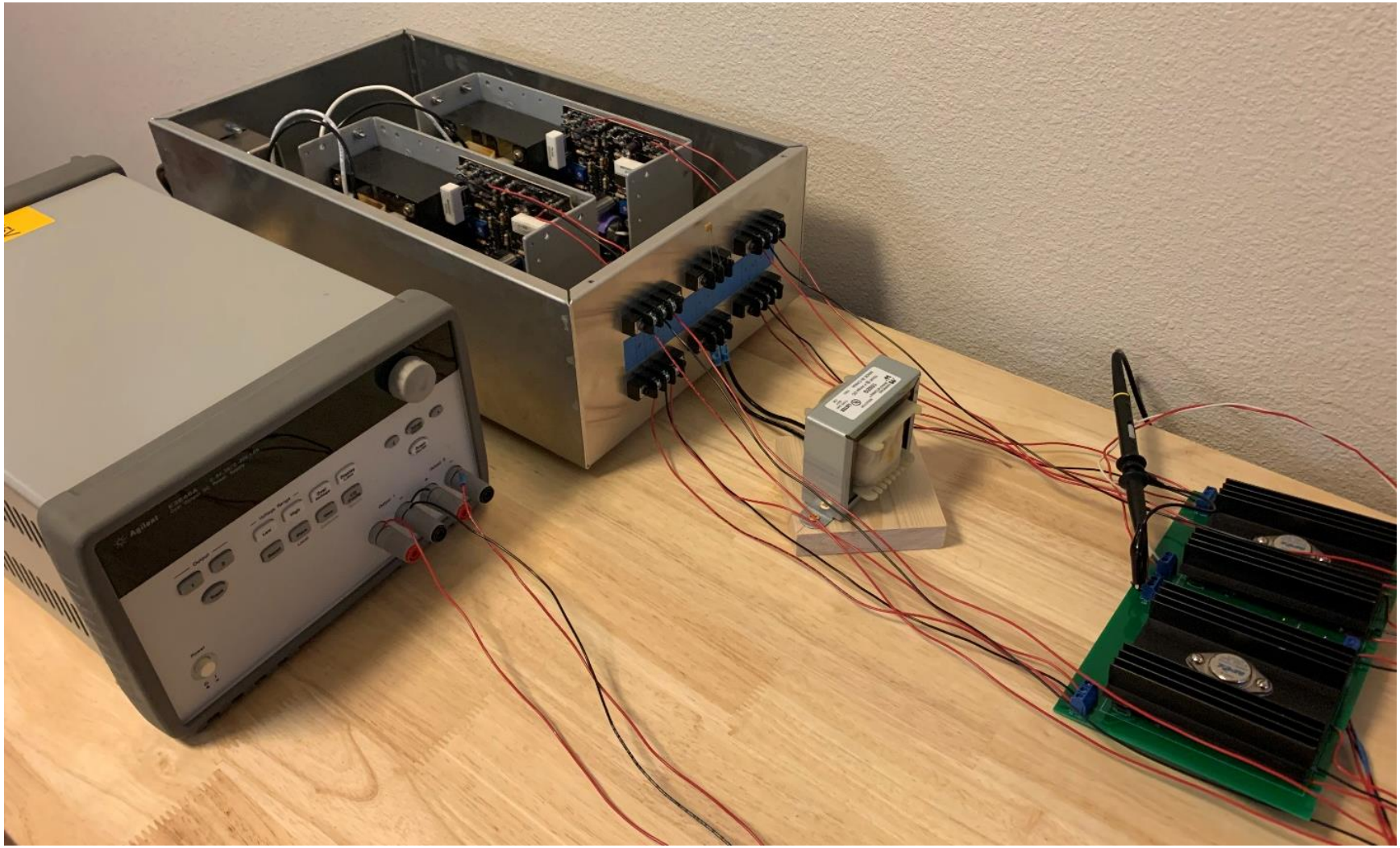

Figure 4.3: Power supply arrangement. The open enclosure contains both of the fixed, linear power supplies used for the transconductance amplifier. The programmable power supply is used to power the modified Pierce oscillator.

4.2.1 Oscillator

Figure 4.4 shows a detailed view of the oscillator portion of the circuit in Figure 4.1. Pins +A and −A connect to the transconductance amplifier portion of the overall circuit. All component values in Figure 4.4 are nominal. A Texas Instruments OPA227 was used for the oscillator op amp. Better choices do exist for this application, but the low-noise performance, high bandwidth, and wide supply range of the OPA227 make it a reasonable choice for a proof of concept. From the data sheet, the OPA227 has a nominal output impedance of 27 Ω. The implementation of the modified Pierce oscillator is shown within the red box in Figure 4.5.

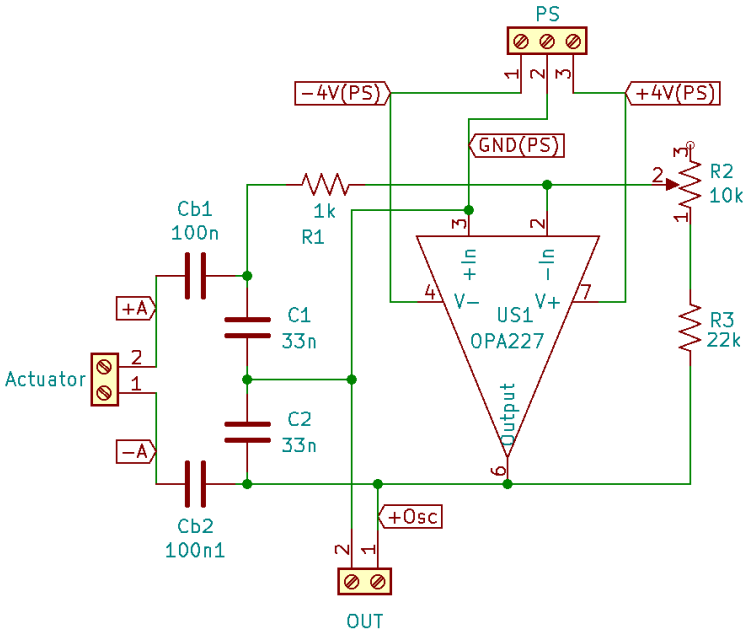

Figure 4.4: Detailed view of the modified Pierce oscillator portion of Figure 4.1. Pins +A and −A connect to the transconductance amplifier portion of the test circuit.

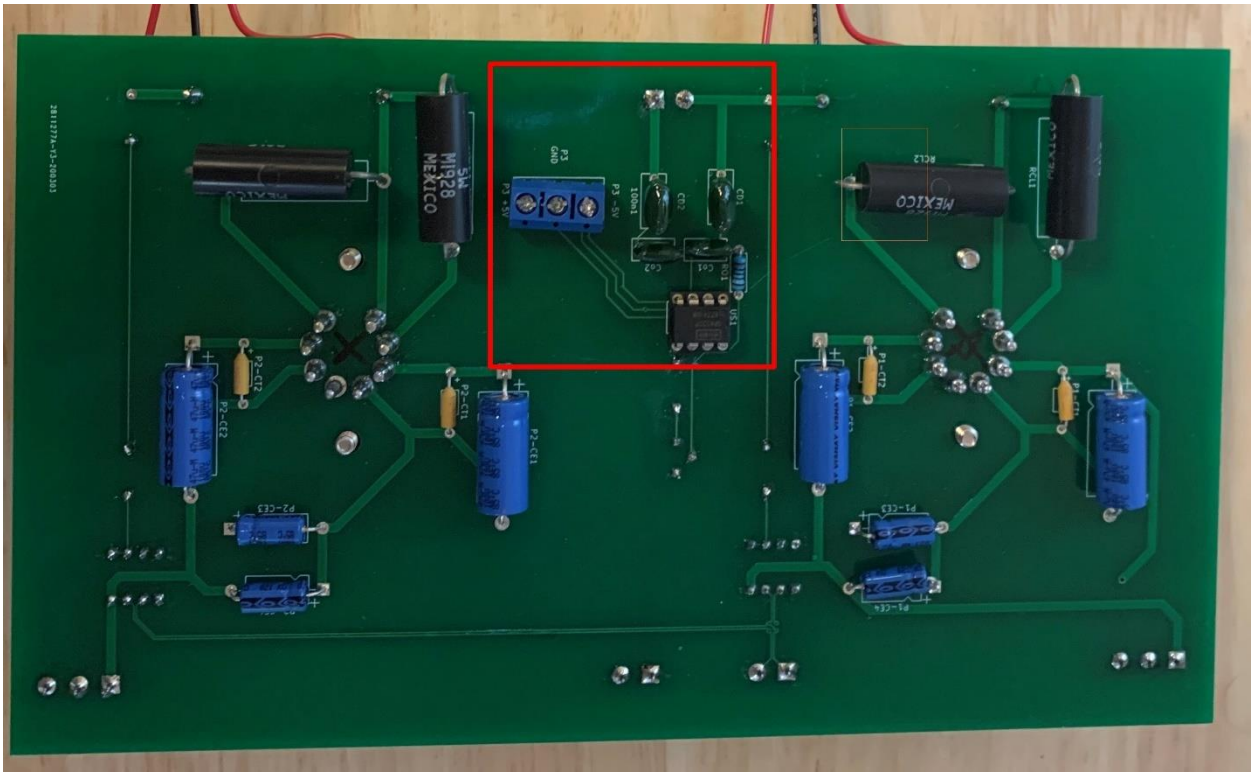

Figure 4.5: Implementation of the modified Pierce oscillator. The red boxed area includes the modified Pierce oscillator components. Note that the potentiometer is on the other side of the circuit board.

4.2.1.1 Variable Inductor

A variable inductor was used in place of a PIVI actuator. Ideally, an actuator would have also been used to test the modified Pierce oscillator. However, a significant amount of development time was spent on mitigating parasitic capacitance in the transconductance amplifier. Because of this, there was not sufficient time to test the system with an actual actuator as well. The variable inductor, shown in Figure 4.6, consists of a solenoid with a movable permeable core.

The solenoid is a single-layer, cylindrical winding formed on a paperboard tube. The winding is made with 237 turns of 30-gauge enamel copper wire and measures 69 mm long and 24 mm in

diameter. The series resistance of the solenoid was measured at 6.8 ±0.3 Ω.

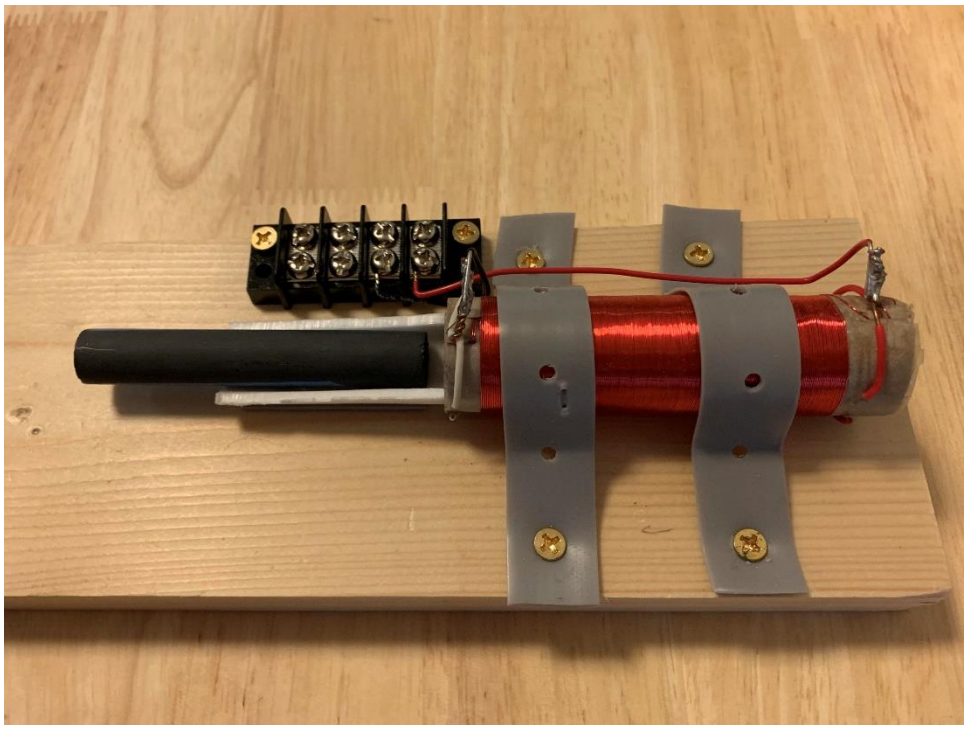

Figure 4.6: Image of the variable inductor. The core position markings are not visible.

The core is made of a MnZn ferrite rod that is 75 mm long and 12 mm in diameter. This material was chosen because of its high relative permeability, approximately 600, and low conductivity. Low conductivity was considered desirable for reducing eddy current losses at high frequencies. The core is marked at 5 mm increments along its length. The insertion distance of the core is set/measured by aligning these markings with the left edge of the paperboard tube. The edge of the paperboard tube is offset from the edge of the solenoid windings by 7 mm, so the 0 mm position of the core markings is offset by 7 mm in order to align the edges of the solenoid and core. The result of this is that the position range of the core is from 0 mm to 65 mm. This is shown in Figure 4.7.

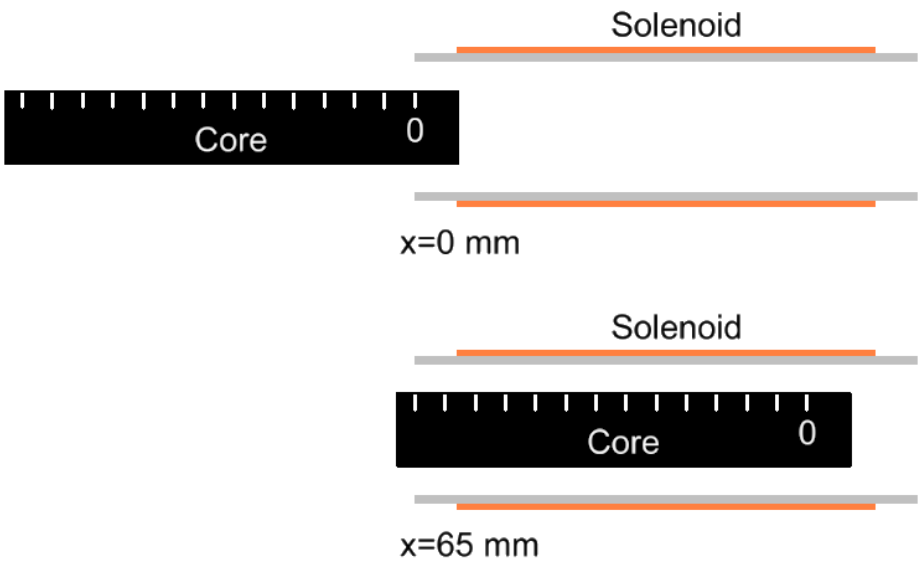

Figure 4.7: Depiction of the core-insertion-distance measurement methodology. The core-insertion distance markings are shown in white on the core. The paperboard tube is shown in gray. Top: The core is set at 0 mm insertion distance. This is considered to be the minimum position because the right edge of the core and the left edge of the solenoid are aligned. Bottom: The core is set to 65 mm insertion distance. This is considered to be the maximum position because this is the last mark available with 5 mm spacing.

Unlike the E-core actuator example, this variable inductor cannot be easily modeled primarily due to the lack of a well-defined magnetic circuit in the design. For simplicity, the inductance was instead measured experimentally. This was achieved by constructing a low-pass filter with the variable inductor and studying its frequency response. The methodology used for this process can be found in Appendix A. The resulting regression equation between inductance and core-insertion is shown in (4.1). A fourth-order regression equation was used because it was the lowest-order polynomial regression that offered a reasonable residual error.

$$L_A(x) = (-9.127 \times 10^{-5})x^4 + (5.899 \times 10^{-3})x^3 + (45.56)x + 440.7 \qquad (4.1)$$

where x is the core-insertion distance in millimeters and $L_A(x)$ is the inductance in microhenries. Note that (4.1) is only valid for insertion positions from 0 mm to 65 mm. Figure 4.8 shows a plot

of (4.1) as a function of core-insertion position. As discussed in Section 3.4.1, under the low-frequency assumption, a PIVI actuator can be modeled as a variable inductor with a strictly monotonic relationship between inductance and actuator position.

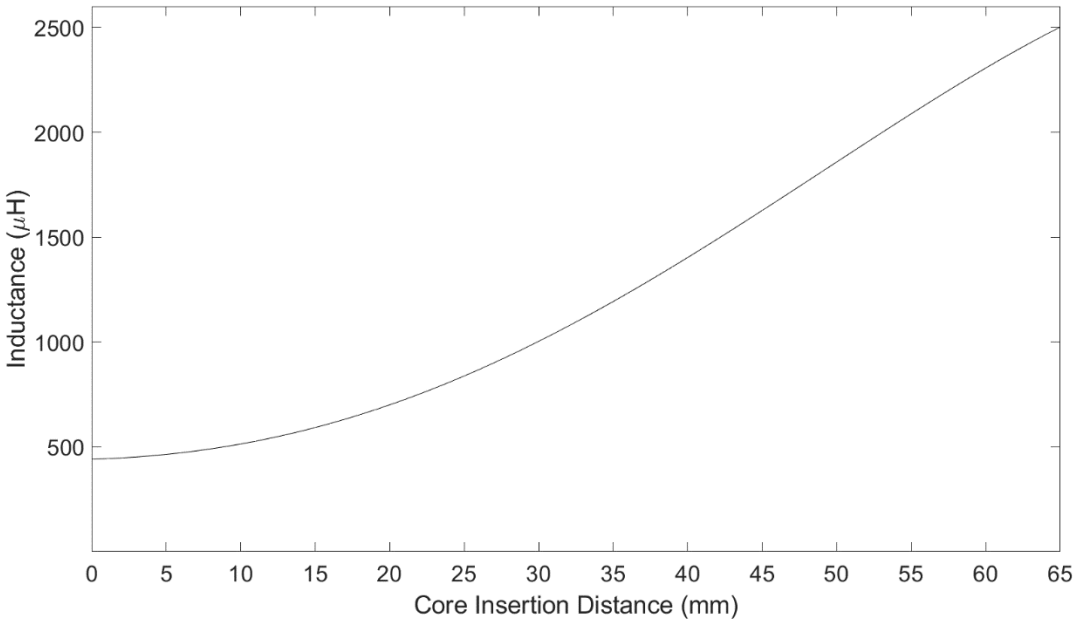

Figure 4.8: Plot of inductance vs. core-insertion distance for the variable inductor. This plot is constructed from (4.1).

From Figure 4.8, it is clear that the constructed variable inductor has a strictly monotonic relationship between inductance and core-insertion position. Therefore, under the low-frequency assumption, the constructed variable inductor serves as an analog of a PIVI actuator. Consequently, while not an ideal test specimen, the variable inductor was considered good enough for proof of concept tests of the modified Pierce oscillator.

4.2.1.2 Fundamental Frequency and Gain

The component values for the oscillator circuit are summarized in Table 4.1. The measurement

uncertainty is derived from the specifications of the Fluke 179 multimeter used to measure the component values.

Table 4.1: Summary of oscillator component values.

Component	Nominal	Measured	Unit
R_a	n/a	6.8 ±0.3	Ω
R_o	27	n/a	Ω
C_1	33	34 ±2	nF
C_2	33	35 ±2	nF
C_{b1}	100	100 ±3	nF
C_{b2}	100	102 ±3	nF
R_1	1k	0.994k ±10	Ω
R_2	10k	9.47k ±86	Ω
R_3	22k	21.86k ±210	Ω

The measured component values in Table 4.1 and (3.73), (3.74), and (4.1) are used to estimate the predicted fundamental frequency of the oscillator as a function of core position. This relationship is plotted in Figure 4.9. Figure 4.9 shows that, as expected from Section 3.4.2, the predicted relationship between fundamental oscillation frequency and core position is strictly monotonic. From Figure 4.9, the predicted oscillator frequency-band can be estimated to be approximately 30 kHz to 70 kHz over the expected range of inductance.

The gain condition in (3.91) is modified to include the potentiometer resistance. The result is (4.2).

$$\frac{R_2 + R_3}{R_1} = -A_{vo} \geq C_1 R_A \left(\frac{R_A}{L_A} + \frac{1}{R_o C_2} + \frac{R_o C_2}{L_A C_T} \right) + \frac{C_1}{C_2} \tag{4.2}$$

The measured component values in Table 4.1 and (3.74) and (4.2) are used to estimate the required feedback gain. The required gain varies with inductance, but the maximum gain is calculated from

the minimum inductance as 1.26. This does provide a theoretical estimate for the minimum required feedback gain. However, in practice, the gain was set to a much higher value: 31.5. Such a high value was required because oscillations were not found to be self-sustaining at all core positions when a lower gain was used. It is unknown exactly why such a high gain value was required to ensure self-sustaining oscillations at all core positions. However, it is possible that the op amp dynamics, which were not included in the analysis of the modified Pierce oscillator, played a significant role in the disagreement of between prediction and implementation. Other possible culprits include the lack of automatic gain control and the capacitive load at the output of the OPA227. The former likely led to nonlinear behavior in the oscillator while the latter may have altered the dynamic response of the op amp.

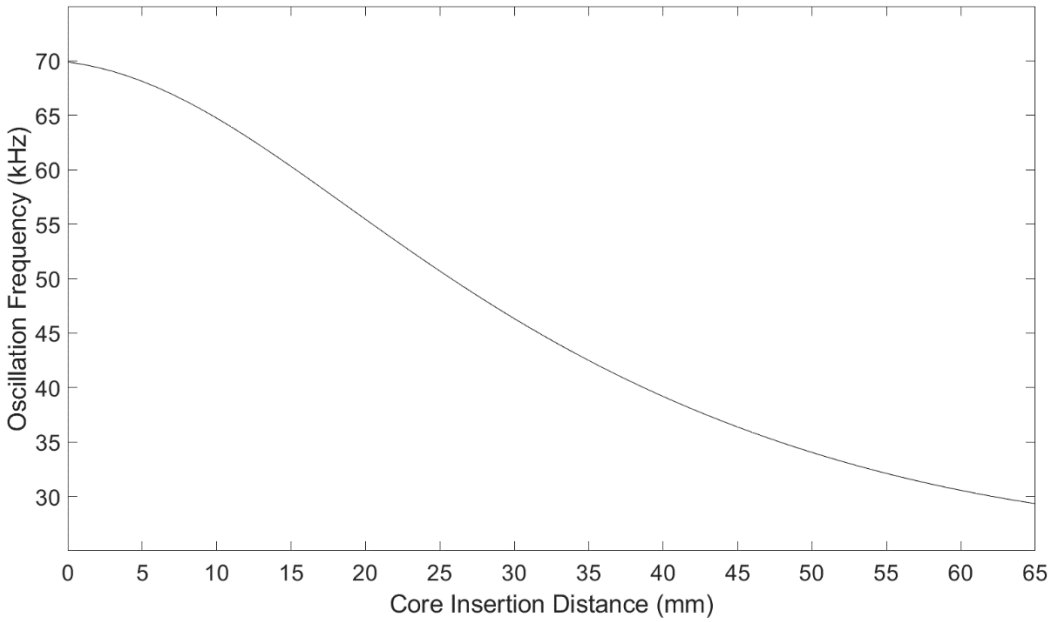

Figure 4.9: Predicted fundamental oscillation frequency of the modified Pierce oscillator as a function of core-insertion distance.

4.2.2 Transconductance Amplifier

Figure 4.10 shows a detailed view of the transconductance amplifier. Pins +A and −A connect to the oscillator portion of this circuit. The implementation of this circuit is shown in Figure 4.11.

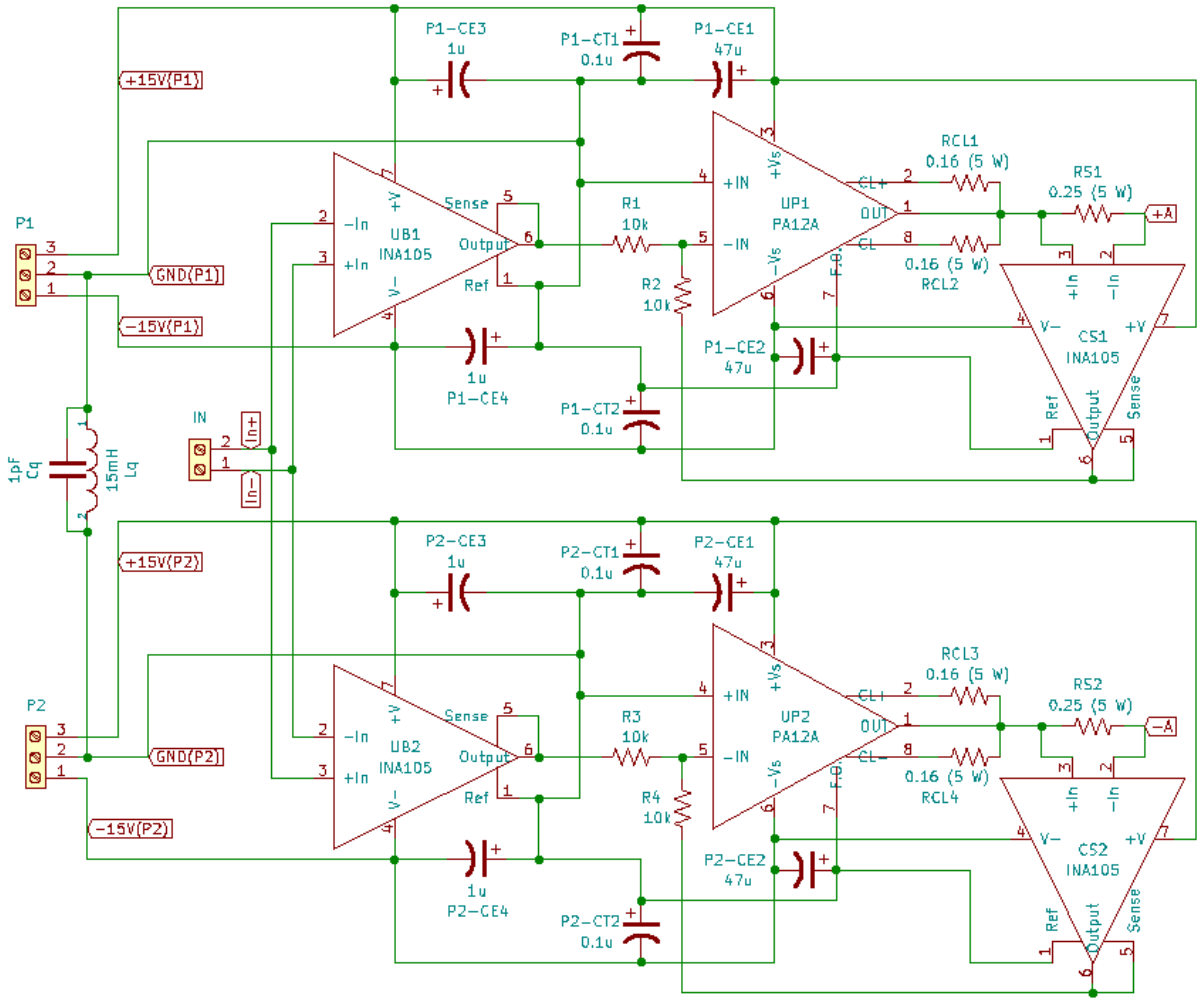

Figure 4.10: Detailed view of the transconductance amplifier portion of Figure 4.1. Pins +A and −A connect to the modified Pierce oscillator portion of the test circuit.

The complexity of this design stemmed from the use of the Apex PA12A power op amp. This particular component was chosen for two primary reasons. First, the use of this component, or

indeed any power op amp, greatly simplified the design of the transconductance amplifier by eliminating the design of the power amplifier stage. Second, this particular power op amp was already available, so it would have been more expensive to order a different power op amp. In spite of those reasons, the PA12A is not an ideal choice for this application due to the existence of significant parasitic capacitance between its output pin and power supply rails. When disconnected from the power supply and the power supply decoupling capacitors, this parasitic capacitance was measured at 3 ±2 nF between the positive rail and OUT and 13 ±2 nF between the negative rail and OUT.

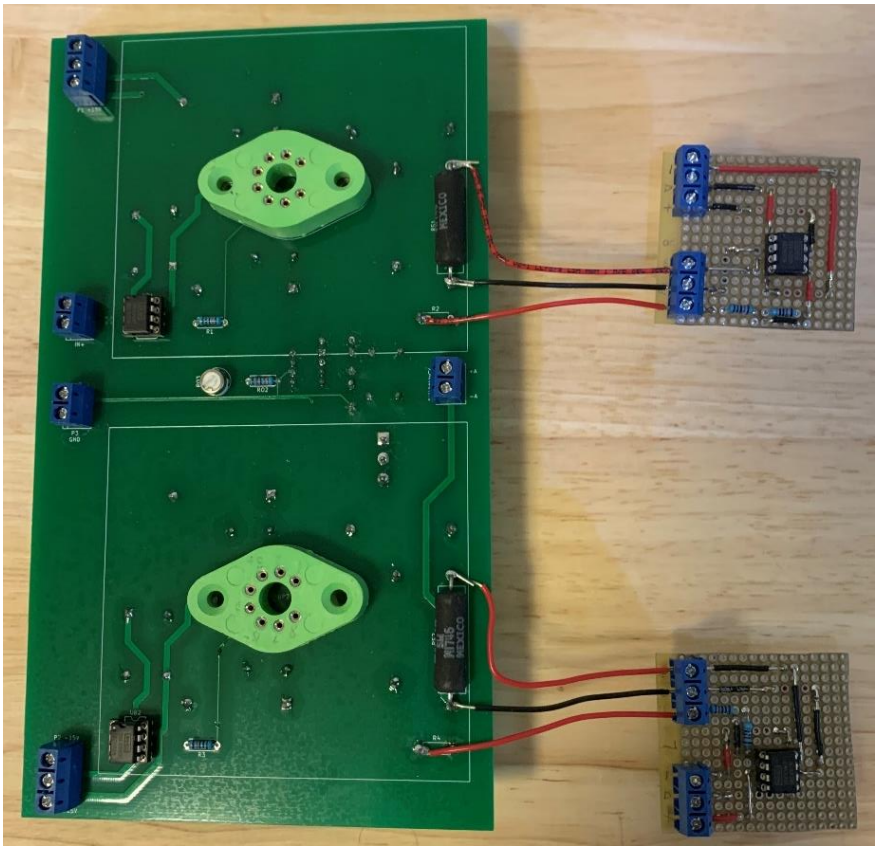

Figure 4.11: Implementation of the transconductance amplifier. The PA12A amplifiers and heat sinks have been removed to better show the circuit elements. The external circuit boards contain the current sense amplifiers. Note that the modified Pierce oscillator is located on the opposite side of the board.

This capacitance is of a similar order of magnitude to the capacitance of the capacitors used for the oscillator circuit. So, this parasitic capacitance can affect the fundamental frequency of the oscillator. This effect is best demonstrated in the conventional transconductance amplifier shown in Figure 4.12.

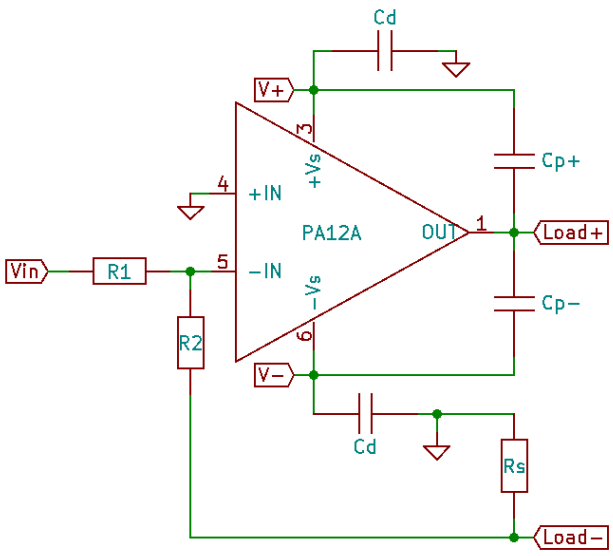

Figure 4.12: Depiction of a conventional transconductance amplifier with parasitic capacitance.

Where capacitors C_{p+} and C_{p-} represent the parasitic capacitance of the PA12A, and capacitors C_d are the power supply decoupling capacitors. The power supply decoupling capacitors are included in this circuit because they are the primary reason the parasitic capacitance is an issue. If the high-impedance components of the circuit are removed, as shown in Figure 4.13, it can clearly be seen that the power supply decoupling capacitors provide a link to ground for the parasitic capacitance. If it is assumed that the capacitance of each power supply decoupling capacitor is much larger than the parasitic capacitance, then the series capacitance will be dominated by the parasitic capacitance. As a result, the parasitic capacitance is effectively placed in parallel with the

load of the amplifier. It is clear that, if this conventional transconductance amplifier was used with the modified Pierce oscillator, the parasitic capacitance would affect the fundamental frequency of the oscillator.

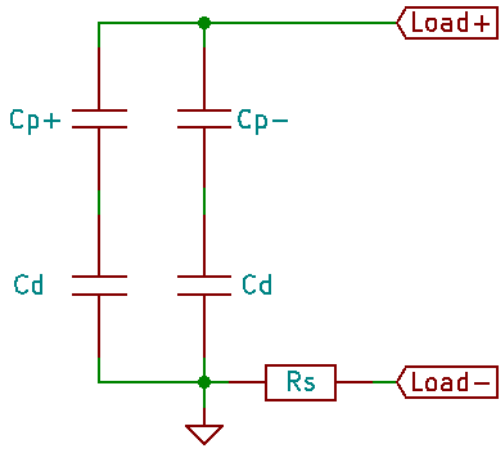

Figure 4.13: Parallel circuit elements from Figure 4.12. The sense resistor R_s is assumed to have a resistance less than or equal to 1 Ω. This is small enough to be considered negligible when analyzing the parasitic capacitance.

Additionally, since there is no guarantee that the parasitic capacitance will be constant with varying amplifier excitation, it is possible that the relationship between the fundamental frequency of the oscillator and the position of the inductor core would be dependent on the state of the transconductance amplifier.

Therefore, in order to reduce the effect of this parasitic capacitance, the transconductance amplifier in Figure 4.10 was constructed with two transconductance amplifiers in a push-pull configuration. This push-pull configuration uses two separate power supplies, one for each stage, that are connected through their grounds. The result of this design is that the parasitic capacitance is halved

to 8 nF in parallel with the load. Further mitigation of parasitic capacitance was achieved by linking the grounds of the separate push-pull stages through the compensation circuit described in Section 3.5.1. As discussed previously, the impedance of the compensated path, formed by the series combination of L_q, C_q, and the parasitic capacitance, can be increased above that of the parasitic capacitance alone within the oscillator frequency-band by proper selection of components. Proper selection of components also allows the impedance of the compensated path to be increased well above that of the actuator's inductance. This behavior is shown in Figure 4.14, where the magnitude of the theoretical impedance of the parasitic capacitance, compensated path, and variable inductor are compared.

The magnitude of the theoretical impedance of the parasitic capacitance was computed from the magnitude of the impedance of a capacitor, $\frac{1}{\omega C}$, and a nominal parasitic capacitance of 8 nF. Half of the total parasitic capacitance was used due to the mitigation effect of the push-pull topology. The magnitude of the theoretical impedance of the compensated path was computed from the magnitude of (3.98), a nominal value of 15 mH and measured value of 0.15 ±0.2 Ω for L_q, a nominal value of 1 pF for C_q, and a nominal parasitic capacitance of 8 nF. The magnitude of the theoretical impedance of the variable inductor was computed from the magnitude of the impedance of an inductor and series resistance $\sqrt{(R_a)^2 + (\omega L_a)^2}$. A measured value of 6.8 ±0.3 Ω was used for R_a. Since the inductance of the variable inductor controls the oscillation frequency, and is therefore not constant, the maximum measured inductance, 2.5 mH, and the minimum measured inductance, 441 µH, were used to calculate the impedance at the bounds of the oscillator frequency-band. That is to say, the maximum inductance provides the impedance at 30 kHz and the minimum inductance provides the impedance at 70 kHz .

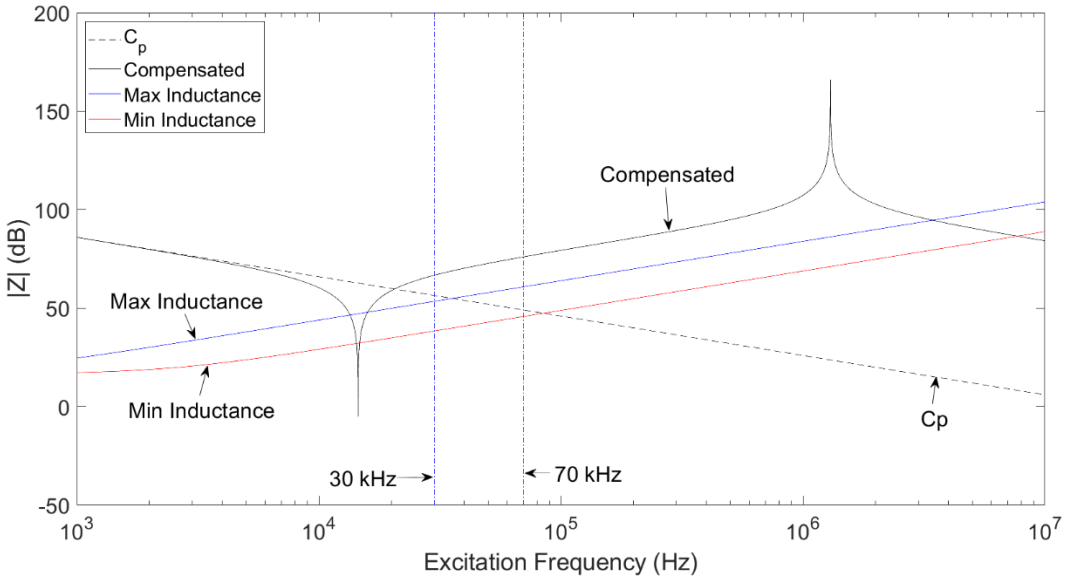

Figure 4.14: Comparison of the magnitude of theoretical impedance of the parasitic capacitance, compensated path, and variable inductor. The predicted frequency-band of the oscillator is enclosed between the vertical lines at 30 kHz and 70 kHz. The MATLAB script used to generate this plot can be found in Appendix B.

It is clear from Figure 4.14 that the theoretical impedance of the compensated path is greatly increased above that of the parasitic capacitance alone. Additionally, due to the selection of L_q and C_q, the theoretical impedance of the compensated path is increased greatly above that of the variable inductor within the oscillator frequency-band. This increase in theoretical impedance at the bounds of the oscillator frequency-band is summarized in Table 4.2. As discussed in Section 3.5.1, the result of this increased impedance is a theoretical reduction of the effect of parasitic capacitance on the fundamental frequency of the modified Pierce oscillator.

Table 4.2: Summary of theoretical impedances at the oscillator frequency-band boundaries.

Frequency	Parasitic Capacitance Impedance (8 nF)	Compensated Path Impedance	Variable Inductor Impedance
30 kHz	663 Ω	2.16 kΩ	471 Ω
70 kHz	285 Ω	6.31 kΩ	194 Ω

A consequence of this amplifier design is the potential for nonuniformity in the amplifier gain due to component mismatch between the separate transconductance amplifier stages. This issue was observed in the implementation of the overall circuit. Figure 4.15 shows the measured DC gain and the 4 A/V design gain.

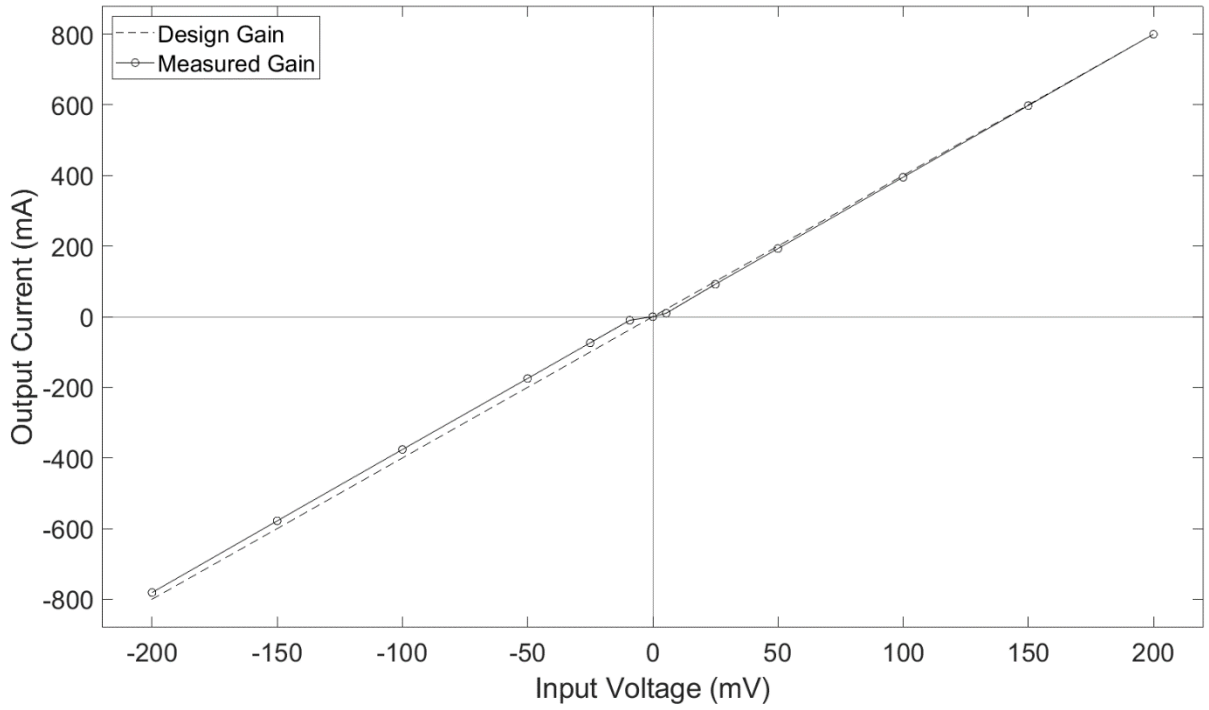

Figure 4.15: Comparison of design gain with measured transconductance amplifier gain.

The deadband and offset seen in the third quadrant are likely a result of both amplifiers not

conducting at the same time. This can likely be attributed to the existence of a bias voltage in one or more of the INA105 differential amplifiers or either of the PA12A amplifiers used in this design. This distortion could be improved with the addition of trimming components, the use of proportional-integral (PI) feedback, or even the use of an application-made amplifier. However, the measured gain is reasonably linear and close to the design gain. Therefore, it was considered good enough for a proof of concept.

4.3 Experimental Procedure

The overall test setup is shown in Figure 4.16. In order to show the viability of the modified Pierce oscillator for self-sensing applications, the test circuit was tested under conditions that approximate an actively powered PIVI voice-coil actuator. This was achieved by using the transconductance amplifier to apply disturbance currents through the variable inductor in order to simulate a powered actuator. The relationship between oscillation frequency and core-insertion distance was then determined over the range of core positions. The primary objective of these disturbance tests was to show that the oscillator's fundamental frequency is not affected by disturbance current through the variable inductor as long as the disturbance current obeys the low-frequency assumption. The implication of this behavior is that the core-insertion distance of the variable inductor can still be determined from oscillation frequency even when a disturbance current is applied to the variable inductor.

4.3.1 Test Conditions

The transconductance amplifier was controlled with input from a function generator. The function generator was built into the Keysight DSOX1102G digital storage oscilloscope used for data collection. Four excitation inputs were tested with the transconductance amplifier. The first test

used a 0-V input to the transconductance amplifier. This quiescent-output test was conducted to provide a comparison baseline for all other tests since it represents a realistic calibration condition for the system.

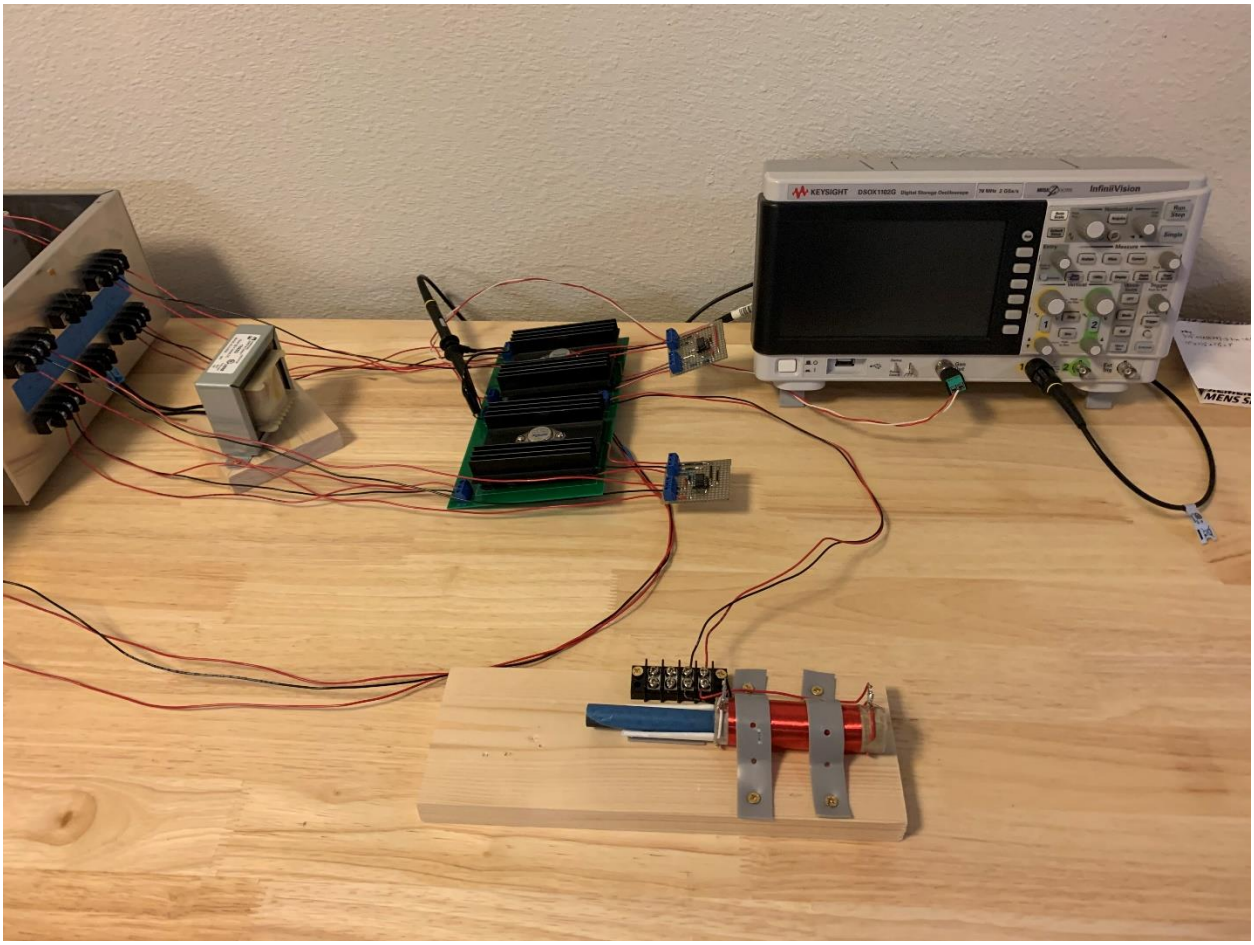

Figure 4.16: View of full test setup.

The remaining disturbance tests were conducted with the following inputs: A DC input of 100 mV, a 100-mV sine-wave input at 100 Hz, and a 100-mV square-wave input at 100 Hz. These inputs were chosen to provide a variety of disturbance currents through the variable inductor.

A special case was also tested with the circuit where the modified Pierce oscillator was separated from the transconductance amplifier. This was done by removing the PA12A amplifiers from their sockets, disconnecting the power supplies of the transconductance amplifier stages, and disconnecting components L_q and C_q. This test was conducted both to determine the effect of parasitic capacitance on the oscillation frequency and to provide a more direct comparison with the theoretical prediction.

4.3.2 Data Collection

The data collection process was the same for every test case. First, the core-insertion position of the variable inductor was adjusted to the 0-mm position. Then, the output waveform of the modified Pierce oscillator was recorded with the Keysight DSOX1102G digital storage oscilloscope. Next, the core-insertion distance was increased by 5 mm, and the output of the modified Pierce oscillator was recorded again. This process was repeated for every 5 mm step from 0 mm to 65 mm of core-insertion.

The core-insertion distance was manually aligned during each run. With a resolution of one mark per 5 mm, the position uncertainty during the core position sweep could theoretically be as high as ±2.5 mm. This level of uncertainty is not ideal, but it was considered good enough for a proof of concept. The digital storage oscilloscope was setup to save 5000 data points for each capture. This was the maximum data capture size available for the Keysight DSOX1102G. Additionally, the horizontal scale of the oscilloscope was adjusted to ensure that at least thirteen complete oscillation cycles were visible before the data was captured. This was done to ensure a constant number of cycles were available for frequency determination regardless of oscillation frequency.

The captured oscilloscope data was analyzed in MATLAB. The scripts used to analyze the data can be found in Appendix C. For each tested position, a zero-crossing detector algorithm was applied to the captured oscillator waveform. The oscillation frequency was then determined at every full cycle in the captured waveform. That is to say, the oscillation frequencies were measured from both the period between every adjacent negative to positive transition and the period between every adjacent positive to negative transition. This was done because the measured waveform was not uniform over a full cycle. Therefore, measuring frequency from every half cycle would have resulted in a bimodal distribution of measured frequencies for a given position. Next, all measured frequencies outside of a 25 kHz to 75 kHz frequency-band were rejected. This was done to remove high-frequency spikes from the ends of the oscillator waveform. The 25 kHz to 75 kHz band was chosen to allow for variations outside of the expected oscillator frequency-band. Finally, the average was taken from the remaining measured frequencies. This average frequency was considered to be the oscillation frequency for a given position. The standard error was also estimated from the remaining measured frequencies using the sample standard deviation.

4.4 Results

4.4.1 Disturbance Rejection

The results of the excitation tests are shown in Figure 4.17. Note that the error bars are computed from the estimated standard error. As expected, the relationship between oscillation frequency and core-insertion distance was strictly monotonic in all excitation tests. Additionally, the variation in oscillation frequency between the excitation tests was quite low. This is quantified in Figure 4.18, where the percentage error of each excitation test from the quiescent-output test is plotted. At maximum, the percentage error of any of the excitation tests from the quiescent-output test was

less than 3%. The consistency between the excitation tests suggests that the disturbance current through the variable inductor had little effect on the oscillation frequency of the modified Pierce oscillator.

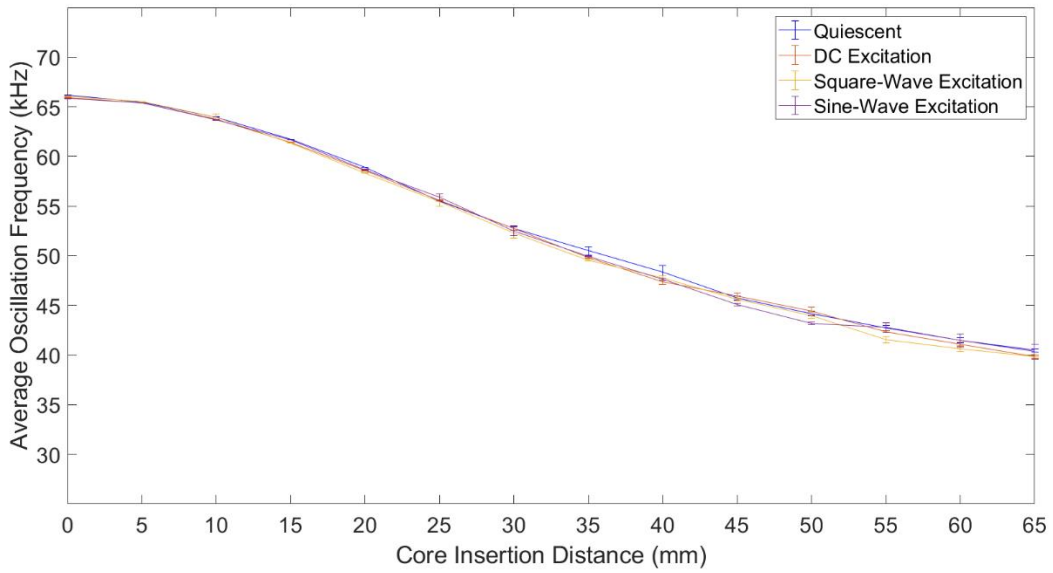

Figure 4.17: Comparison of oscillation frequency as a function of core-insertion distance from all four excitation tests.

Consequently, it should be possible to determine the insertion distance of the core from the oscillation frequency of the modified Pierce oscillator even in the presence of disturbance currents through the variable inductor. These conditions simulated a PIVI actuator both under the low-frequency assumption and powered by a current source. It is therefore considered likely that this modified Pierce oscillator could be used for self-sensing with a PIVI actuator that is both operated within the low-frequency assumption and powered by a current source. However, while these results are promising, they are not definitive. Further tests with an actual PIVI actuator will be needed to determine the effectiveness of this self-sensing methodology.

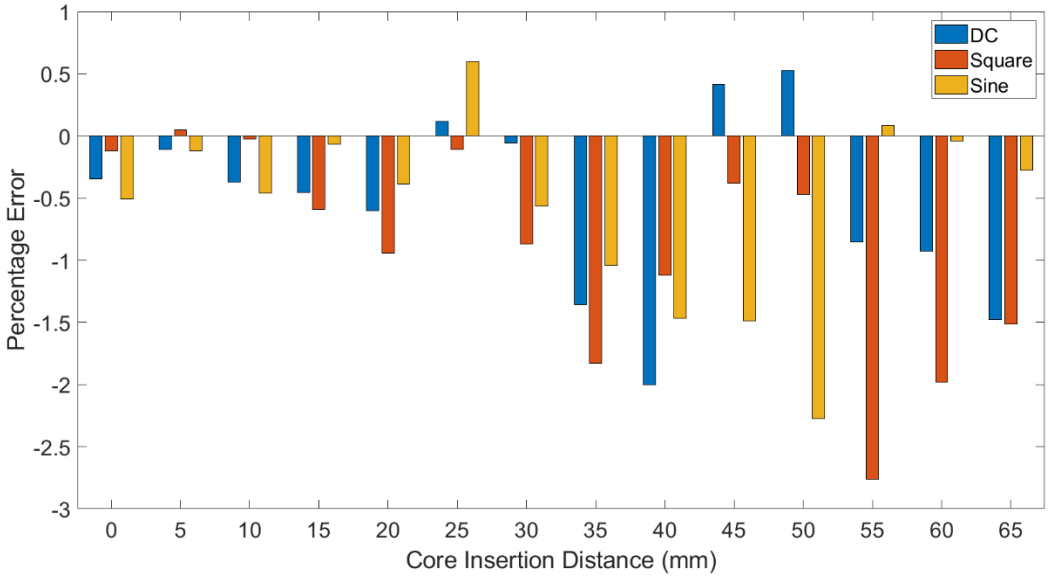

Figure 4.18: Comparison of the percentage error of the DC, sine-wave, and square-wave excitation tests from the quiescent-output test.

4.4.2 Prediction Accuracy

The results of the free-oscillation and quiescent-output tests are compared with the predicted free-oscillation frequency in Figure 4.19. It is clear that there was significant disagreement between the prediction and both the free-oscillation and quiescent-output tests. This is quantified in Figure 4.20, which plots the percentage error of both tests from the predicted oscillation frequency. This significant discrepancy suggests that the analysis of the modified Pierce oscillator was not detailed enough to accurately predict the behavior in the free-oscillation test, and that the transconductance amplifier dynamics had a significant effect on the oscillation frequency in the quiescent-output test. Prediction accuracy could be further improved with the addition of both the op amp dynamics and transconductance amplifier dynamics. However, the increased complexity from adding these dynamics into the modeling process would likely preclude an analytical solution to the Barkhausen criterion. This is more specifically the case when the transconductance amplifier dynamics are

considered. A numerical analysis of the circuit may therefore be necessary if a more accurate prediction is needed.

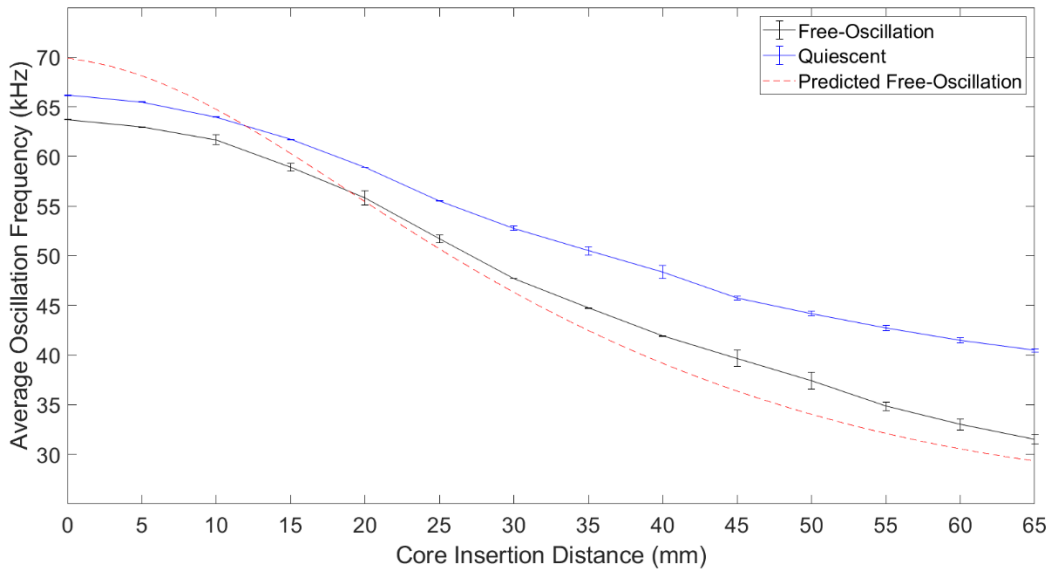

Figure 4.19: Comparison of oscillation frequency as a function of core-insertion distance from the free-oscillation test, quiescent-output test, and predicted fundamental oscillation frequency.

4.5 Practical Limitations

While the modified Pierce oscillator performed well in the tested configuration, it should be acknowledged that this self-sensing methodology is not without limitations. There are several issues that can arise when this modified Pierce oscillator, or indeed any derivative of this design, is used with a real PIVI voice-coil actuator. One particularly important issue stems from the effect of core saturation in a real PIVI voice-coil actuator. That is to say, a high enough current through the PIVI actuator windings can lead to a decrease in the permeability of the actuator core due to magnetic saturation. This will affect the inductance relationship of the actuator and, by extension,

the fundamental frequency of the oscillator. Therefore, use of the modified Pierce oscillator for self-sensing would likely require a derating factor on the maximum control current applied to the actuator. This would help prevent saturation of the core and ensure the oscillation frequency is invariant to the control current. Alternatively, if the current through the actuator is monitored during operation, a lookup table, like the one discussed in [1], could be developed and used to account for shifts in the frequency-band due to saturation. The effectiveness of this strategy would likely depend on the effect of saturation on the resolution of the frequency vs. position relationship.

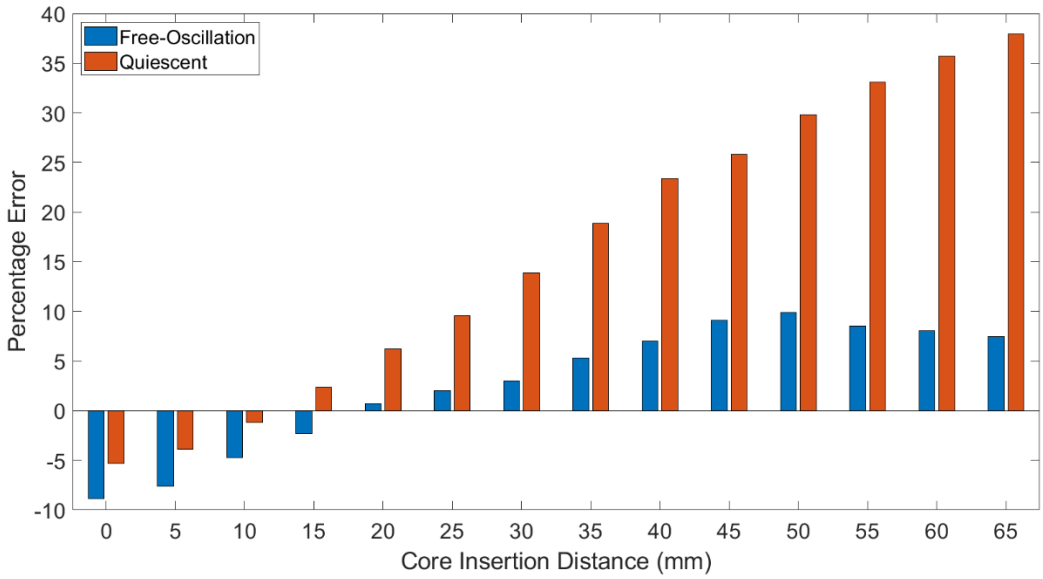

Figure 4.20: Comparison of the percentage error of the quiescent-output test and free-oscillation test from the predicted fundamental oscillation frequency.

Another important issue arises from the frequency-dependent properties of the actuator core. Most real voice-coil actuators, PIVI or otherwise, have cores that exhibit complex permeability behavior and experience eddy current losses. Both of these behaviors tend to be more pronounced at higher frequencies, so they tend to place an upper limit on the oscillation frequency that can be achieved

with a real actuator. Depending on the type of PIVI voice-coil actuator, this limit may severely restrict the amount of bandwidth available for the oscillator and actuator. Therefore, use of the modified Pierce oscillator for self-sensing would likely be restricted to actuators with both low eddy current losses and fairly constant core permeability in the oscillator frequency-band. Even with this restriction, the control current and actuator bandwidth would still need to be constrained by the low-frequency assumption. Both of these limitations, and the issues that require them, are all the more reason why this self-sensing methodology requires further testing with a real PIVI voice-coil actuator.

5. SUMMARY AND CONCLUSIONS

5.1 Summary

A generalized electrical model of PIVI actuators was first derived to motivate the development of a self-sensing methodology. Basic oscillator theory was then presented and applied to a typical Pierce oscillator. A modified Pierce oscillator was then introduced for self-sensing applications. The low-frequency assumption, a constraint on the maximum frequency of motion and current input, was defined in order to simplify the analysis of the modified Pierce oscillator. The predicted behavior of this modified Pierce oscillator, a fundamental oscillation frequency that is a strictly monotonic function of actuator inductance, was presented as the motivating reason for using this oscillator for self-sensing. The effects of parasitic capacitance in the actuator current source were then discussed along with a mitigation method. A test circuit, including the modified Pierce oscillator and a transconductance amplifier, was presented. Due to time constraints, the modified Pierce oscillator was constructed with a variable inductor rather than an actual PIVI actuator. This was considered acceptable since the variable inductor mimics a PIVI actuator operating under the low-frequency assumption. Modifications to the transconductance amplifier were presented that allowed parasitic impedance to be increased by a minimum factor of three. The test circuit was tested under conditions that simulated the disturbance currents of a powered PIVI actuator in order to determine the performance of the modified Pierce oscillator. Finally, some practical limitations of the modified Pierce oscillator were discussed.

5.2 Conclusions

Experimental validation with the test circuit showed that the oscillation frequency of the modified Pierce oscillator was a strictly monotonic function of the core-insertion distance of the variable

inductor. The result of this behavior was that the core-insertion distance could be uniquely determined from the oscillation frequency of the modified Pierce oscillator. Since the variable inductor simulated a PIVI actuator under the slow motion assumption, it was considered likely that this behavior would also have been observed with a PIVI actuator operating within the low-frequency assumption. It was also observed that the oscillation frequency of the modified Pierce oscillator was fairly consistent in the presence of disturbance current through the variable inductor. In the presence of DC, sine-wave, and square-wave disturbance current, the oscillation frequency stayed with 3% of the quiescent oscillation frequency over the range of motion of the actuator. These conditions simulated a powered PIVI actuator, so it is conceivable that the oscillation frequency would also be fairly consistent if the modified Pierce oscillator was used with an actual PIVI actuator. While these results are not definitive, they suggest that the modified Pierce oscillator, or indeed a derivative of it, could be used as a self-sensing methodology for PIVI type voice-coil actuators. However, more work will be needed to verify this behavior with an actual PIVI type voice-coil actuator.

6. FUTURE WORK

In order to validate the performance of the modified Pierce oscillator, the system should be tested with an actual PIVI voice-coil actuator under power and motion. This will allow the observation of the effects of back emf and core losses in a more realistic setting. Inversion of the frequency-position curve should also be pursued with the ultimate goal being full position-feedback control using the oscillator output.

A simpler transconductance amplifier topology should be developed for a more practical implementation. This could be achieved by using a single transconductance amplifier stage, rather than the push-pull design used here, with the parasitic-capacitance-mitigation components in series with the actuator. This would greatly reduce the complexity of the design, and reduce the required power supplies to two. A better implementation of the modified Pierce oscillator should also be pursued. The inclusion of dynamic gain control could significantly improve the predictability and frequency stability of the oscillator. Additionally, if frequency stability can be improved, then a much smaller frequency-band could be used for the oscillator without affecting position resolution.

REFERENCES

[1] M. F. Rahman, N. C. Cheung, and K. W. Lim, "Position estimation in solenoid actuators," *IEEE Transactions on Industry Applications*, vol. 32, no. 3, pp. 552–559, May-June 1996, doi: 10.1109/28.502166.

[2] S. Wu and W. N. Chen, "Self-sensing of a solenoid valve via phase detection," *2009 IEEE/ASME International Conference on Advanced Intelligent Mechatronics*, Singapore, September 2009, pp. 1165–1170, doi: 10.1109/AIM.2009.5229744.

[3] S. I. Moore and S. O. R. Moheimani, "Displacement Measurement With a Self-Sensing MEMS Electrostatic Drive," *Journal of Microelectromechanical Systems*, vol. 23, no. 3, pp. 511–513, June 2014, doi: 10.1109/JMEMS.2014.2314296.

[4] H. H. Woodson and J. R. Melcher, *Electromechanical Dynamics, Part I: Discrete Systems*. New York, NY: John Wiley and Sons, 1968.

[5] G. Gonzalez, *Foundations of Oscillator Circuit Design*. Boston, MA: Artech House, 2007.

[6] G. F. Franklin, J. D. Powell, and A. Emami-Naeini, *Feedback Control of Dynamic Systems* (7th ed.). Upper Saddle River, NJ: Pearson, 2015.

[7] L. Meirovitch, *Fundamentals of Vibrations*. Boston, MA: McGraw-Hill, 2001.

[8] H. Nagaoka, "The Inductance Coefficients of Solenoids," *The Journal of the College of Science, Imperial University of Tokyo, Japan*, vol 27, pp. 18-33, August 1909, doi: 10.15083/00037799.

APPENDIX A: EXPERIMENTAL MEASUREMENT OF INDUCTANCE

A.1 Analysis

The inductance of the variable inductor was estimated from the frequency response of a low-pass filter. This filter is shown in Figure A.1.

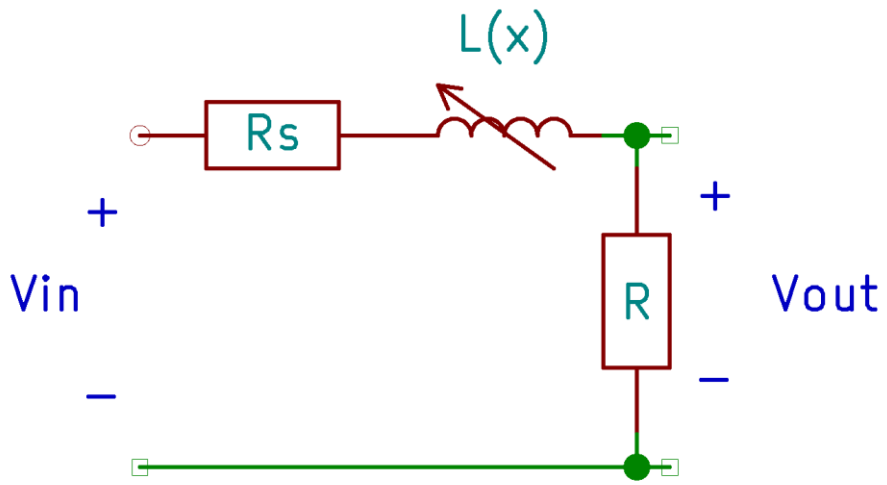

Figure A.1: Circuit diagram of the low-pass filter used to determine inductance.

Where R_s is the series resistance of the inductor and $L(x)$ is the inductance as a function of core position. The impedance of the loop is defined by (A.1).

$$Z_T \triangleq Z_{R_s} + Z_L + Z_R = (R_s + R) + j\omega L(x) \tag{A.1}$$

The current through the loop due to V_{in} is found by applying Ohm's law for reactive circuits.

$$I = \frac{V_{in}}{Z_T} = \frac{V_{in}}{(R_s + R) + j\omega L(x)} \tag{A.2}$$

The output voltage is described by (A.3).

$$V_{out} = IZ_R = IR. \tag{A.3}$$

Substituting (A.2) into (A.3) and solving for the transfer function yields (A.4).

$$\frac{V_{out}}{V_{in}} = G_f = \frac{R}{(R_s + R) + j\omega L(x)} \tag{A.4}$$

Equation (A.4) is rearranged into standard Bode form [6].

$$G_f = K_o \frac{1}{j\frac{\omega}{\omega_b(x)} + 1} \tag{A.5}$$

where the corner frequency and DC gain are defined by (A.6) and (A.7).

$$\omega_b(x) \triangleq \frac{R_s + R}{L(x)} \tag{A.6}$$

$$K_o \triangleq \frac{R}{R_s + R} \tag{A.7}$$

From (A.6), the corner frequency is inversely proportional to the inductance of the variable inductor. Therefore, if the corner frequency of the filter can be experimentally determined, then the inductance can be calculated.

The corner frequency of the filter is most easily found by studying the magnitude and phase angle of the frequency response. To simplify this process, (A.5) is rewritten in terms of its real and imaginary parts.

$$G_f = K_o \frac{1 - j\frac{\omega}{\omega_b(x)}}{\left(\frac{\omega}{\omega_b(x)}\right)^2 + 1} \tag{A.8}$$

The magnitude is now defined as [7]

$$M \triangleq \sqrt{Re\left(G_f\right)^2 + Im\left(G_f\right)^2} \tag{A.9}$$

Substituting the real and imaginary parts of (A.8) into (A.9) yields (A.10).

$$M(\omega, x) = \sqrt{\left(\frac{K_o}{\left(\frac{\omega}{\omega_b(x)}\right)^2 + 1}\right)^2 + \left(\frac{-K_o \frac{\omega}{\omega_b(x)}}{\left(\frac{\omega}{\omega_b(x)}\right)^2 + 1}\right)^2} \tag{A.10}$$

Equation (A.10) simplifies to (A.11).

$$M(\omega, x) = \frac{|K_o|}{\sqrt{\left(\frac{\omega}{\omega_b(x)}\right)^2 + 1}} \tag{A.11}$$

Applying the field power definition [6] to (A.11) yields (A.12).

$$M_f(\omega, x) = 20 \log_{10}\left(\frac{|K_o|}{\sqrt{\left(\frac{\omega}{\omega_b(x)}\right)^2 + 1}}\right) \tag{A.12}$$

The real part of (A.8) is positive by definition, so the phase angle of the frequency response can be defined in terms of the arctangent function rather than the two-argument arctangent function [7].

$$\phi \triangleq \tan^{-1}\left(\frac{Im\left(G_f\right)}{Re\left(G_f\right)}\right) \tag{A.13}$$

Substituting the real and imaginary parts of (A.8) into (A.13) yields (A.14).

$$\phi(\omega, x) = \tan^{-1}\left(\frac{-K_o \dfrac{\omega}{\omega_b(x)}}{\left(\dfrac{\omega}{\omega_b(x)}\right)^2 + 1} \frac{\left(\dfrac{\omega}{\omega_b(x)}\right)^2 + 1}{K_o}\right) \tag{A.14}$$

Equation (A.14) simplifies to (A.15).

$$\phi(\omega, x) = -\tan^{-1}\left(\frac{\omega}{\omega_b(x)}\right) \tag{A.15}$$

Equation (A.12) and (A.15) describe the theoretical frequency response of the filter. In the case where $\omega = \omega_b(x)$, (A.12) and (A.15) yield the following identities.

$$M_f = 20\log_{10}\left(\frac{|K_o|}{\sqrt{2}}\right) = 20\log_{10}\left(\frac{R}{\sqrt{2}(R_s + R)}\right) \tag{A.16}$$

$$\phi = -\tan^{-1}(1) = -45° \tag{A.17}$$

If the frequency response of the filter is known experimentally, then the corner frequency can be estimated from the excitation frequency that satisfies either (A.16) or (A.17). The inductance is then found by solving (A.6) with the estimated corner frequency.

In reality, a discrete set of excitation frequencies is tested, so the excitation frequency will never exactly match the corner frequency of the filter. This limits the usefulness of (A.16) and (A.17), so the experimental frequency response of the filter must be related to (A.12) or (A.15). All things being equal, the phase angle is a much simpler relationship than the Magnitude. Equation (A.15) is rewritten as (A.18).

$$\omega_b(x) = \frac{-\omega}{\tan\left(\phi_e(\omega, x)\right)} \tag{A.18}$$

where $\phi_e(\omega, x)$ is the experimentally determined phase response. Substituting (A.6) and solving

for the inductance yields (A.19).

$$L(x) = \frac{-\tan\left(\phi_e(\omega_e, x)\right)(R_s + R)}{\omega_e} = \frac{-\tan\left(\phi_e(\omega_e, x)\right)(R_s + R)}{2\pi f_e} \tag{A.19}$$

Equation (A.19) can be used to relate the experimental phase response of the filter to the inductance of the inductor. It is theoretically possible to find the inductance from the experimental phase response using an arbitrary excitation frequency. However, on an *x*-axis, semi-log plot, the phase angle versus excitation frequency is most sensitive near the point where the condition in (A.15) is met. It will therefore be better to use (A.19) with excitation frequencies that result in a phase angle close to −45º.

A.2 Experimental Procedure and Measured Inductance

The low-pass filter in Figure A.1 was constructed with the variable inductor. The series resistance of the inductor was measured at 6.8 ±0.05 Ω. The filter resistor was set to a nominal value of 100 Ω and had a measured value of 100 ±0.05 Ω.

The core of the variable inductor was marked at 5 mm increments from 0 mm of insertion to 65 mm of insertion. This was the same marking system shown in Figure 4.7. Starting at 0 mm core-insertion, the filter was excited with a 0.5-Vpp sine-wave. The phase response of the filter was then recorded over a frequency sweep from 100 Hz to 10 kHz at 50 points per decade. From the discrete test points, an excitation frequency was chosen that resulted in a phase angle as close to −45º as possible. This excitation frequency and phase angle were then used to find the inductance from (A.19). This process was repeated for each 5 mm increment of core-insertion. The results are shown in Table A.1.

The air core inductance was also determined to be 427 µH using the same test procedure with the core removed. From [8], the self-inductance of a cylindrical, single-layer, air-core solenoid is described by (A.20).

$$L_a = K\frac{\mu_0 N^2 A}{L} \tag{A.20}$$

Where N is the number of turns, A is the cross sectional area of the solenoid, L is the length of the solenoid, and K is the Nagaoka coefficient. For a diameter to length ratio of 0.348, the Nagaoka coefficient is approximately 0.866 [8]. This results in an estimated air-core inductance of 401 µH. The measured value was within 7% of this estimated value, so the experimental results were considered to be reasonable.

Table A.1: Summary of experimental inductance data.

Core Insertion (mm)	Excitation Frequency (kHz)	Phase Angle (Deg)	Calculated Inductance (µH)
0	38.0	−44.61	441.0
5	36.3	−44.82	465.2
10	33.1	−44.98	513.0
15	28.8	−45.02	589.8
20	25.1	−45.58	690.5
25	20.0	−44.78	845.5
30	16.6	−44.84	1018
35	14.5	−45.36	1191
40	12.0	−44.56	1393
45	10.5	−44.89	1617
50	91.2	−45.00	1864
55	79.4	−44.38	2094
60	72.4	−44.51	2307
65	69.2	−45.48	2499

Using the experimental data in Table A.1, a fourth-order polynomial regression was applied to the

relationship between the calculated inductance, in microhenries, and the core-insertion distance, in millimeters. The resulting regression equation is shown in (A.21). Note that (A.21) is the same as (4.1).

$$L_A(x) = (-9.127 \times 10^{-5})x^4 + (5.899 \times 10^{-3})x^3 + (45.56)x + 440.7 \qquad \text{(A.21)}$$

A polynomial regression was pursued because both the analysis in Section 2 and earlier finite element analysis indicated that the relationship may be polynomial in nature. A fourth-order regression was chosen because it was the lowest-order polynomial regression that offered a reasonable residual error. Figure A.2 shows a comparison plot of the regression equation and the discrete test data.

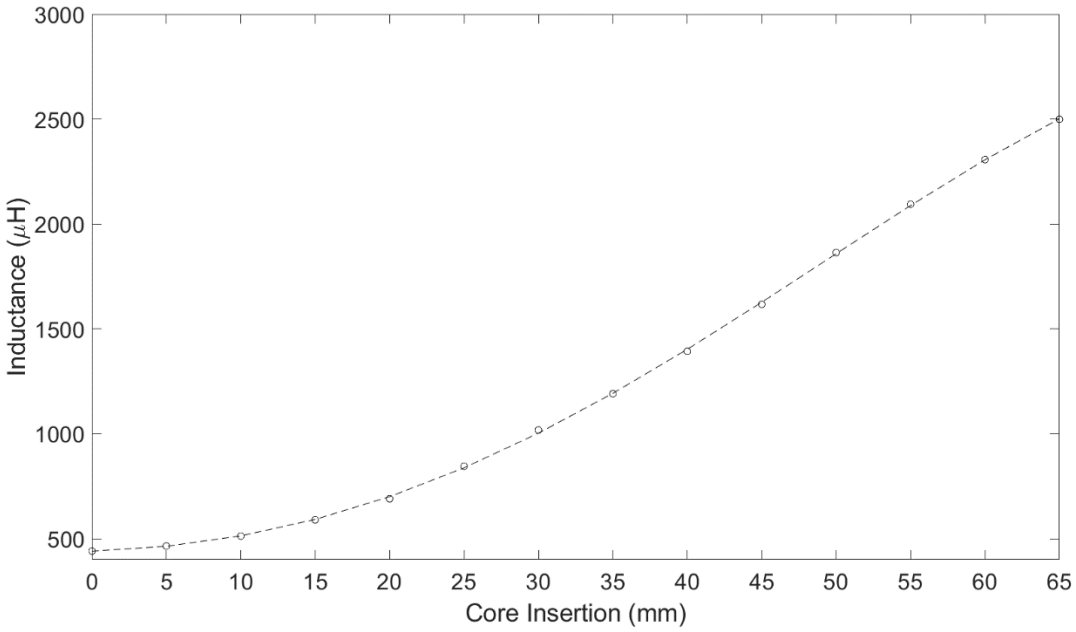

Figure A.2: Comparison of regression equation with test data from Table A.1.

APPENDIX B: THEORETICAL IMPEDANCE PLOT GENERATION

```
% Parameters
Cp=8e-9;
q=length(Cp);
Lq=15e-3;
Rq=0.15;
Cq=1e-12;
b=10000;
f1=3;
f2=7;
f=logspace(f1,f2,b);
w=2*pi.*f;

% Impedance Calculation
Z_Cp=zeros(q,b);
Z_TR=zeros(q,b);
Z_OL=zeros(q,b);
Z_OH=zeros(q,b);
for k=1:q
    Z_Cp(k,:)=1./(1j.*w.*Cp(k));
    Z_TR(k,:)=((1j.*w).^2.*Lq.*(Cq+Cp(k))+(1j*w).*Rq.*(Cq+Cp(k))+1)./((1j*w.*
C p(k)).*((1j*w).^2.*Lq.*Cq+(1j*w).*Rq.*Cq+1));
    Z_OL=6.8+1j.*w.*2.5e-3;
    Z_OH=6.8+1j.*w.*441e-6;
end

% Magnitude Calculation
M_Cp=Bode_P(Z_Cp);
M_TR=Bode_P(Z_TR);
M_ZOL=Bode_P(Z_OL);
M_ZOH=Bode_P(Z_OH);

% Plotting
close all
semilogx(f,20*log10(M_Cp),'Color','k','LineStyle','--')
hold on
semilogx(f,20*log10(M_TR),'Color','k','LineStyle','-')
semilogx(f,20*log10(M_ZOL),'Color','b','LineStyle','-')
semilogx(f,20*log10(M_ZOH),'Color','r','LineStyle','-')
plot(30e3.*ones(1,b),linspace(-50,200,b),'Color','b','LineStyle','-.')
plot(70e3.*ones(1,b),linspace(-50,200,b),'Color','r','LineStyle','-.')
xlabel('Excitation Frequency (Hz)')
ylabel('|Z| (dB)')
ylim([-50,200])
legend({'C_p','Compensated','Max Inductance','Min
Inductance'},'location','northwest')
set(gca,'Fontsize',20)

% Magnitude and Phase Angle Function
function [M,P]=Bode_P(G)
    M=sqrt(real(G).^2+imag(G).^2);
    P=atan2d(imag(G),real(G));
end
```

APPENDIX C: MATLAB DATA REDUCTION SCRIPT

```
% Data Loading
close all
if exist('D','var')~=1
    clear
    load Run_Data.mat
end
%Data Reduction Loop
q=size(D);
Avg=zeros(q(1),14);
err=zeros(q(1),14);
for p=1:q(1)
    for i=2:15
        %Zero-Crossing Detector
        k=length(D(p,i,:,:))-1;
        c=0;
        for j=1:length(D(p,i,:,:))-1
            if (D(p,i,j,2)==0) || (D(p,i,j,2)>0 && D(p,i,j+1,2)<0) ||
(D(p,i,j,2)<0 && D(p,i,j+1,2)>0)
                c=c+1;
                k(c)=D(p,i,j,1);
            end
        end
        k=k(1:c);

        %Frequency Determination
        A=zeros(c-1,1);
        for j=2:c-1
            A(j)=1/(1*(k(j+1)-k(j-1)));
            %Frequency calculated between every two zero-crossings
        end

        %Cutoff Window
        Ac=zeros(c-1,1);
        cf=0;
        for j=1:c-1
            if A(j)<75e3 && A(j)>25e3
                cf=cf+1;
                Ac(cf)=A(j);
            end
        end

       %Frequency Average and Standard Error
        Avg(p,i-1)=sum(Ac)/(cf);
        err(p,i-1)=std(Ac(1:cf))/sqrt(cf);
            %Used for error bars in plots
    end
end
```